

**NUMERICAL ANALYSIS OF NOVEL MINI CHANNEL
COOLING PLATE FOR CYLINDRICAL LITHIUM-ION
BATTERY PACK**

A DISSERTATION

SUBMITTED IN PARTIAL FULFILLMENT OF THE REQUIREMENTS
FOR THE AWARD OF THE DEGREE
OF

MASTER OF TECHNOLOGY
IN
THERMAL ENGINEERING

Submitted by:

MD DANISH KHAN

(2K21/THE/20)

Under the supervision of

Dr. MOHAMMAD ZUNAID



**DEPARTMENT OF MECHANICAL ENGINEERING
DELHI TECHNOLOGICAL UNIVERSITY**
(Formerly Delhi College of Engineering)
Bawana Road, Delhi-110042

MAY, 2023

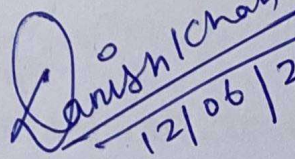
DELHI TECHNOLOGICAL UNIVERSITY
(Formerly Delhi College of Engineering)
Bawana Road, Delhi-110042

CANDIDATE DECLARATION

I, MD DANISH KHAN, Roll No. 2K21/THE/20 student of M.Tech-Thermal Engineering, hereby declare that the project Dissertation titled "NUMERICAL ANALYSIS OF NOVEL MINI CHANNEL COOLING PLATE FOR CYLINDRICAL LITHIUM-ION BATTERY PACK" which is submitted by me to the Department of Mechanical Engineering, Delhi Technological University, Delhi in partial fulfilment of the requirement for the award of the degree of Master of Technology, is original and not copied from any source without proper citation. This work has not previously formed the basis for the award of any Degree, Diploma Associateship, Fellowship or other similar title or recognition.

Place: Delhi

Date: 12/06/2023


12/06/2023

MD DANISH KHAN

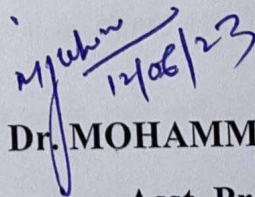
DEPARTMENT OF MECHANICAL ENGINEERING
DELHI TECHNOLOGICAL UNIVERSITY
(Formerly Delhi College of Engineering)
Bawana Road, Delhi-110042

CERTIFICATE

I hereby certify that the Project Dissertation titled "NUMERICAL ANALYSIS OF NOVEL MINI CHANNEL COOLING PLATE FOR CYLINDRICAL LITHIUM-ION BATTERY PACK" which is submitted by **MD Danish Khan**, Roll No. **2K21/THE/20**, Department of Mechanical Engineering, Delhi Technological University, Delhi in partial fulfilment of the requirement for the award of the degree of Master of Technology, is a record of the project work carried out by the students under my supervision. To the best of knowledge this work has not been submitted in part or full for any Degree or Diploma to this University or elsewhere.

Place: Delhi

Date: 12/06/2023


Dr. MOHAMMAD ZUNAID
Asst. Professor
SUPERVISOR

ABSTRACT

Lithium batteries are broadly utilized in electric vehicles (EVs) and their execution is exceedingly subordinate on temperature. As a result, an efficient battery temperature management system is required to ensure the safe and efficient functioning of EVs. Battery Thermal Management System plays a vital role in keeping up the ideal temperature and temperature distinction of a lithium-ion battery pack, ensuring superior performance, prolonged cycle life, and safety. The growing demand for high-performance and reliable battery packs has necessitated the development of effective cooling systems to mitigate thermal issues and enhance battery performance and safety. The cooling plate design comprises multiple mini channels, which are responsible for extracting heat generated during battery operation. While liquid cooling has been extensively researched for prismatic cells, there has been little research on its application for round and hollow cells (cylindrical cells). Moreover, existing studies on liquid cooling for cylindrical cells primarily focus on flow rate, flow direction, and the number of channels. In this study, a numerical analysis using computational fluid dynamics was carried out on a micro channel cooling plate created for a cylindrical lithium-ion battery pack with forty (40) cells. To investigate the impact of flow velocity, Reynolds number on the conveyance of cell temperature and pressure within the system for 3C and 4C discharge rate, a three-dimensional model of the battery pack is subjected to a numerical analysis using computational fluid dynamics (CFD). The findings indicate that modifying flow directions in the mini-channels improves thermal performance. In particular, when the inlet and outlet are divaricated in each cooling plate using the innovative mini-channel design, the temperature difference can be reduced by 51.67% & 40.46% for 3C and 4C discharge rates, respectively, when compared to unidirectional flow. The implemented battery pack

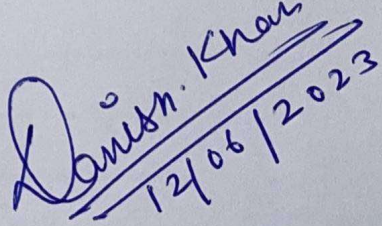
successfully limits the maximum temperature and temperature variation (T.D) to 301.6 K & 3.45 K, respectively, for a 3 C discharge rate and 302.4 K and 4.25 K, under a 4 C discharge rate. These results offer knowledge on improving thermal performance and preserving temperature uniformity, which is useful in the design and enhancement of cylindrical battery cells liquid cooling and thermal management systems.

ACKNOWLEDGEMENT

I would like to express my sincere gratitude to my guide, **Dr. M. Zunaid**, Assistant Professor in the Department of Mechanical Engineering, for his invaluable guidance, support, and expertise throughout the course of this research project. His constant encouragement, insightful feedback, and dedication have been instrumental in shaping the direction and progress of this work. His deep knowledge and passion for the subject have inspired me to strive for excellence and explore futuristic as well as sustainable technology in the field of Battery Thermal Management for Electric Vehicle.

I would also like to extend my heartfelt appreciation to **Prof. S K Garg**, Head of the Department of Mechanical Engineering, for his support and encouragement. His vision and leadership have provided a conducive environment for academic and research pursuits. I am grateful for his valuable insights and guidance that have contributed to the overall success of this project.

Lastly, I would like to acknowledge my family and friends for their unwavering support, encouragement, and understanding throughout this research endeavour. Their love, belief in my abilities, and motivation have been the driving force behind my perseverance and determination.


12/06/2023

MD DANISH KHAN

2K21/THE/20

M.Tech (Thermal Engineering)

Delhi Technological University

TABLE OF CONTENTS

| | |
|--|-----|
| CANDIDATE DECLARATION..... | ii |
| CERTIFICATE..... | iii |
| ABSTRACT..... | iv |
| ACKNOWLEDGEMENT..... | vi |
| TABLE OF CONTENTS..... | vii |
| LIST OF TABLES..... | ix |
| LIST OF FIGURES..... | x |
| NOMENCLATURE..... | xi |
| CHAPTER 1..... | 1 |
| INTRODUCTION..... | 1 |
| 1.1 ELECTRIC VEHICLE – AN OVERVIEW..... | 1 |
| 1.1.1 Battery Technology for EV..... | 2 |
| 1.1.2 Hybrid Electric Vehicle..... | 3 |
| 1.1.3 Storage for EVs: Characteristics of Battery packs and Cells..... | 4 |
| 1.2 BATTERY VARIABLES:..... | 4 |
| 1.2.1 Cell electromotive force (EMF)..... | 4 |
| 1.2.2 Charge (or Amp-hour) capacity..... | 5 |
| 1.2.3 Energy stored..... | 6 |
| 1.2.4 Energy capacity..... | 6 |
| 1.2.5 Energy per unit volume..... | 7 |
| 1.3 LITHIUM-ION BATTERY..... | 7 |
| 1.4 BATTERIES IN FUTURE..... | 8 |
| 1.5 OBJECTIVES OF THESIS..... | 10 |
| CHAPTER 2..... | 12 |
| LITERATURE REVIEW..... | 12 |
| CHAPTER 3..... | 16 |
| METHODOLOGY & MODEL DESCRIPTION..... | 16 |
| 3.1 PROBLEM STATEMENT AND GEOMETRY OF BATTERY PACK WITH MINI CHANNEL..... | 16 |
| 3.2 NUMERICAL FORMULATION AND BOUNDARY CONDITIONS..... | 19 |
| 3.2.1 Heat dissipation model..... | 19 |

| | |
|--|----|
| 3.3 ASSUMPTIONS AND BOUNDARY CONDITIONS | 21 |
| 3.3.1 Assumptions | 21 |
| 3.3.2 Governing Equation..... | 21 |
| 3.3.3 Boundary Conditions..... | 23 |
| CHAPTER 4 | 24 |
| VALIDATION AND GRID INDEPENDENCE TEST | 24 |
| 4.1 VALIDATION | 24 |
| 4.2 MESH GENERATION AND GRID INDEPENDENCE TEST | 25 |
| CHAPTER 5 | 27 |
| RESULTS & DISCUSSION..... | 27 |
| 5.1 RESULTS OF MAXIMUM TEMPERATURE, PRESSURE DROP AND FLUID OUTLET TEMP OF BATTERY PACK FOR 3C DISCHARGE RATE UNDER VARYING REYNOLDS NUMBER..... | 27 |
| 5.1.1 Parametric study of Result of Maximum Temperature (T_{max}) for 3C drain rate | 29 |
| 5.1.2 Parametric study of Result of Pressure Drop (ΔP) for 3C..... | 31 |
| 5.1.3 Parametric study of fluid outlet temperature ($T_{c, out}$) | 32 |
| 5.2 RESULTS OF MAXIMUM TEMPERATURE, PRESSURE DROP AND FLUID OUTLET TEMP OF BATTERY PACK FOR 4C DISCHARGE RATE UNDER VARYING REYNOLDS NUMBER..... | 32 |
| 5.2.1 Parametric study of Result of Maximum Temperature (T_{max}) for 4C drain rate | 34 |
| 5.2.2 Parametric study of Result of Pressure Drop (ΔP) for 4C..... | 36 |
| 5.2.3 Parametric study of fluid outlet temperature (T, out) | 36 |
| 5.3 COMPARISON OF MAXIMUM TEMPERATURE (T_{max}) OF CELL SURFACE WITH VARYING REYNOLDS NO. FOR 3C & 4C DISCHARGE RATE | 37 |
| 5.3.1 Explanation of results:..... | 37 |
| 5.4 COMPARISON OF TC (COOLANT OUTLET) TEMP WITH VARYING REYNOLDS NO. FOR 3C & 4C DISCHARGE RATE..... | 38 |
| 5.4.1 Explanation of Results..... | 38 |
| 5.5 COMPARISON OF P.D (PRESSURE DIFFERENCE PA) OF FLUID / COOLANT WITH VARYING FLOW RATE / REYNOLDS NO. FOR 3C & 4C DISCHARGE RATE | 39 |
| 5.5.1 Explanation of Results..... | 40 |
| CHAPTER 6 | 41 |
| CONCLUSIONS | 41 |
| REFERENCES | 43 |

LIST OF TABLES

| | |
|--|----|
| TABLE 3.1 VALUE OF U-SHAPED CHANNEL GEOMETRIC PARAMETERS | 18 |
| TABLE 3.2 THERMOPHYSICAL PROPERTIES OF LITHIUM-ION CELL [28] | 18 |
| TABLE 3.3 MATERIAL PROPERTIES OF ALUMINIUM AND COOLANT | 19 |
| TABLE 3.4 VOLUMETRIC HEAT ENERGY GENERATION FOR VARIOUS DISCHARGE RATES ... | 20 |
| TABLE 4.1 VARIATION ΔT_{MAX} , ACTUAL & ΔT_{MAX} , VALIDATED WITH VELOCITY TO CALCULATE % ERROR | 25 |
| TABLE 5.1 VARIATION OF T_{max} , ΔP AND $T_{c, out}$ WITH Re FOR 3C | 27 |
| TABLE 5.2 VARIATION OF T_{max} , ΔP AND $T_{c, out}$ WITH Re FOR 4C | 32 |

LIST OF FIGURES

| | |
|---|----|
| FIG. 1.1 PRIMARY ELECTRIC VEHICLE POWER TRAIN [3] | 1 |
| FIGURE 1.2 COMPARISON OF VOLUMETRIC ENERGY DENSITY (WH/L) WITH GRAVIMETRIC ENERGY DENSITY (WH/KG) OF PRISMATIC AND CYLINDRICAL CELL [32] | 2 |
| FIG. 1.3 CONCEPTUAL ILLUSTRATION OF HYBRID ELECTRIC DRIVE TRAIN [4] | 3 |
| FIGURE 1.4 SIMPLE EQUIVALENT CIRCUIT MODEL OF A BATTERY [31]..... | 5 |
| FIGURE 1.5 ILLUSTRATION DEMONSTRATING THE FUNDAMENTAL PARTS AND WORKINGS OF A LI-ION CELL [29]..... | 8 |
| FIG. 3.1 3D VIEW OF U-SHAPED CHANNELS WITH BATTERY PACK..... | 17 |
| FIG. 3.2 FRONT VIEW OF GEOMETRY ALONG WITH DIMENSION | 17 |
| FIG. 4.1 VARIATION OF CHANGE IN MAXIMUM TEMPERATURE DIFFERENCE OF ACTUAL AND VALIDATED RESULTS WITH INCREASE IN VELOCITY | 24 |
| FIG. 4.2 POLYHEDRAL MESH WITH 4 MILLION ELEMENTS | 26 |
| FIG. 4.3 GRID INDEPENDENCE TEST..... | 26 |
| FIG. 5.1 TEMPERATURE CONTOURS OF CELLS DURING 3C DRAIN RATE FOR (A) $Re=900$, (B) $Re=1200$, (C) $Re=1500$, (D) $Re=1800$, (E) $Re=2100$ | 28 |
| FIG. 5.2 PRESSURE DROP OF FLUID CHANNEL DURING 3C DRAIN RATE FOR (A) $Re=900$, (B) $Re=1200$, (C) $Re=1500$, (D) $Re=1800$, (E) $Re=2100$ | 30 |
| FIG. 5.3 TEMPERATURE CONTOURS OF CELLS DURING 4C DRAIN RATE FOR (A) $Re=900$, (B) $Re=1200$, (C) $Re=1500$, (D) $Re=1800$, (E) $Re=2100$ | 33 |
| FIG. 5.4 PRESSURE DROP OF FLUID CHANNEL DURING 4C DRAIN RATE FOR (A) $Re=900$, (B) $Re=1200$, (C) $Re=1500$, (D) $Re=1800$, (E) $Re=2100$ | 35 |
| FIG. 5.5 COMPARISON OF MAXIMUM TEMPERATURE OF CELL BY VARYING REYNOLDS NUMBER..... | 37 |
| FIG. 5.6 COMPARISON OF FLUID OUTLET TEMPERATURE BY VARYING REYNOLDS NUMBER | 38 |
| FIG. 5.7 COMPARISON OF PRESSURE DIFFERENCE FOR 3C AND 4C DRAIN RATE WITH VARYING REYNOLDS NUMBER..... | 39 |

NOMENCLATURE

| | |
|-----------------|---|
| d_1 | Inlet/outlet fixed wall thickness (mm) |
| k | Thermal conductivity in (W /m-K) |
| h | Cooling plate height (mm) |
| h_1 | Height of Inlet / outlet in (mm) |
| L | Length of the cooling plate (mm) |
| P | Static pressure (Pa) |
| ΔP | Change in pressure of coolant/ fluid (Pa) |
| T_{\max} | Maximum Temperature of surface of cell (K) |
| T_c | Inlet temperature of coolant (K) |
| t_1 | Cooling plate Thickness |
| t_2 | Wall Thickness of Cooling plate |
| V | Volume of cell (m^3) |
| ρ | Mass density in (kg /m^3) |
| μ | Viscosity of liquid ($kg / m\cdot s$) |
| $\rightarrow v$ | Velocity vector in (m /s) |
| v | Coolant mass flow rate |
| ρ_c | Coolant Mass density (kg /m^3) |
| C_c | Coolant Heat capacity (J /kg) |
| k_c | Thermal conductivity of the coolant in (W /m-K) |
| PCM | Phase-changed material for BTMS |
| PD | Pressure-drop of fluid/coolant in fluid channel |

CHAPTER 1

INTRODUCTION

1.1 ELECTRIC VEHICLE – AN OVERVIEW

The power train consists of three primary elements: electric motor drive, power source, and assistant components. The electromotive propulsion component includes the vehicle management system, energy conversion device, motorized engine, gear system, and propulsion wheels. The energy reservoir component involves the power source itself, along with the energy optimization unit and the energy replenishment unit. Lastly, the supplementary part, consists of the steering control unit, air conditioning unit, and backup energy unit.

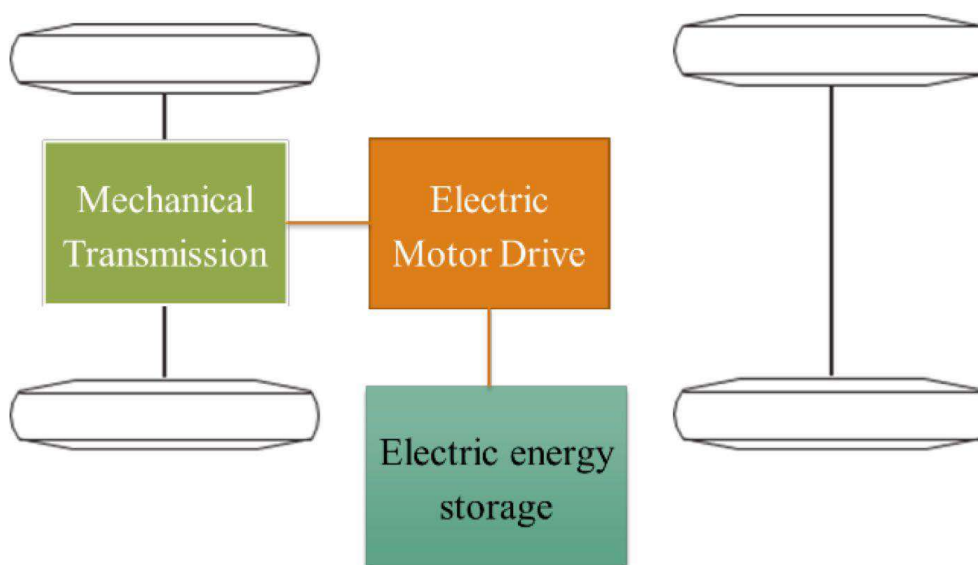


Fig.1.1 Primary Electric vehicle power train [3]

1.1.1 Battery Technology for EV

Compared to liquid fuels, both the gravimetric and volumetric energy densities of batteries are significantly lower. For example, petrol has a volumetric power density of 9375Wh/l as well as gravimetric energy density of 12500Wh/kg. Battery packs typically have a lifespan of 6 to 10 years, with most manufacturers offering an 8-year warranty. The health of a battery depends on determinants such as the rate of charge/discharge, during energizing, depleting, and storage. Optimal working conditions for Li-ion batteries, for occurrence, extend between 25°C & 40°C. State of charge depletion / (DoD) indicates the extent to which the battery is emptied and refilled in each cycle. To maximize the lifespan of a rechargeable battery, it is recommended to avoid fully depleting or fully charging it. Consequently, a battery assembly's useful energy is never greater than its capacity.

Cost of batteries varies depending on their cycle life. Batteries with 500 to 1000 cycles are more affordable, while those with 1500 to 2000 cycles are common and considered medium-cost. Batteries with 3000 to 4000 cycles or more are considered high-cost. Additionally, batteries with fast charge and discharge capabilities are priced significantly higher.

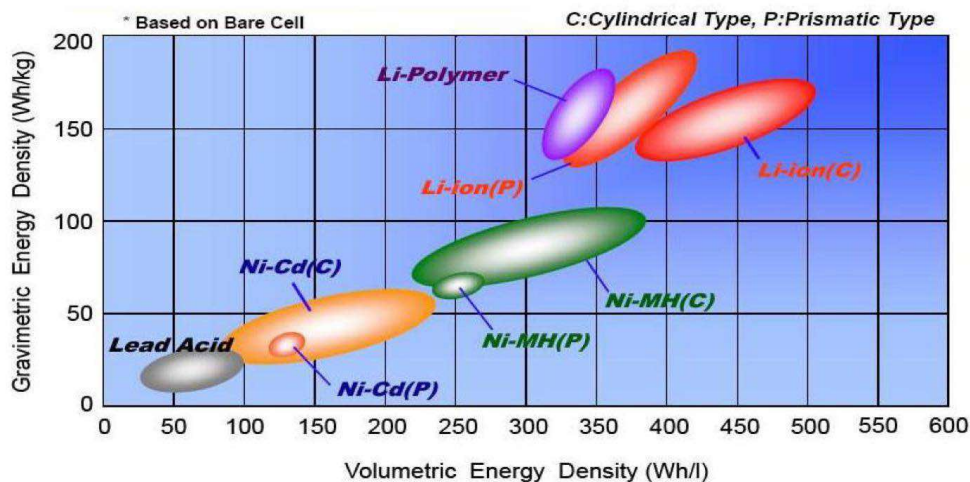


Figure 1.2 Comparison of Volumetric Energy Density (Wh/l) with Gravimetric Energy Density (Wh/kg) of prismatic and cylindrical cell [32]

1.1.2 Hybrid Electric Vehicle

Hybrid electric vehicles (HEVs) combine the benefits of Fossil fuel engine (IC engine) vehicles and electric automobile (EVs), competently overcoming their respective drawbacks. To operate, these vehicles use two power sources: a primary energy source and a secondary energy supply. The combination of the Power generator and the Energy transformer or power source utilized in the vehicle, such as a Combustion engine system, Hydrogen-powered electric motor system, Chemical energy storage system, and so on, is referred to as power transfer. When a vehicle has two or more power trains, it is referred to as a hybrid vehicle, and if it includes an Electric drivetrain, it is specifically called a Hybrid automobile.

The transmission system of a vehicle encompasses all the power trains it incorporates. In order to capture and utilize the braking energy that is typically lost as thermal energy in combustion engine vehicles, combined propulsion system usually include a transmission system that enables bidirectional power distribution. The other power train may be either bidirectional or unidirectional. A crossover drivetrain is outlined to supply control to the stack by selectively using one of the available power trains. By efficiently managing and utilizing the two power trains, several operating patterns are available to satisfy the individual load requirements of the vehicle.

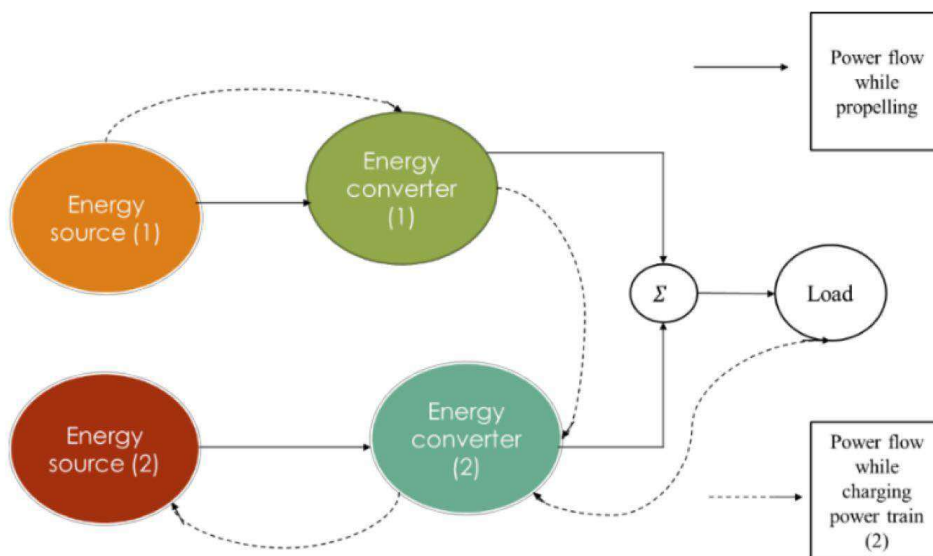


Fig.1.3 Conceptual illustration of hybrid electric drive train [4]

1.1.3 Storage for EVs: Characteristics of Battery packs and Cells

A battery is made up of a few electric cells that are connected together. Chemical energy is changed over into electrical energy by these cells. Each cell is made up of positive and negative terminals associated by an electrolyte. Direct current (DC) power is produced when a chemical response happens between the cathodes and the electrolyte. This chemical response can be turned around within the case of auxiliary or rechargeable batteries by switching the current, permitting the battery to be energized.

From the point of view of an electric vehicle architect, the battery can be considered a "dark box" with different execution criteria. These criteria incorporate particular vitality, vitality thickness, particular control, commonplace voltages, amp-hour proficiency, vitality proficiency, commercial accessibility, fetched, working temperatures, self-discharge rates, number of life cycles, and revive rates. These terms will be advance clarified within the taking after section. Additionally, the originator has to get it how the accessibility of vitality changes in connection to components such as surrounding temperature, charge and release rates, battery geometry, ideal temperature, charging strategies, cooling necessities, and potential future progressions.

1.2 BATTERY VARIABLES:

1.2.1 Cell electromotive force (EMF)

Each electric cell has an apparent voltage that corresponds to the assumed voltage it conveys when generating electrical power. These cells can be linked together in an arrangement to achieve the needed general voltage. Footing batteries for electric vehicles are generally specified as either 6 V or 12 V, and these individual units are linked in order to achieve the desired voltage. Regardless, it's critical to remember that the actual voltage will change in hone. When the battery discharges, the voltage decreases, and when it is charged, the voltage increases. This behaviour is best understood in terms of "inside resistance," which is discussed in the same circuit of a battery shown in Figure 1.3. In this circuit, the battery is identified as having a fixed voltage, denoted as E . Regardless, the voltage measured at the battery terminals is distinct, denoted as V , due to the close proximity to the inner resistance, denoted as R . Assuming that a current, denoted as I , is

flowing out of the battery, as shown in Figure 1.3, the fundamental circuit hypothesis states that:

$$V = IR \quad (1.1)$$

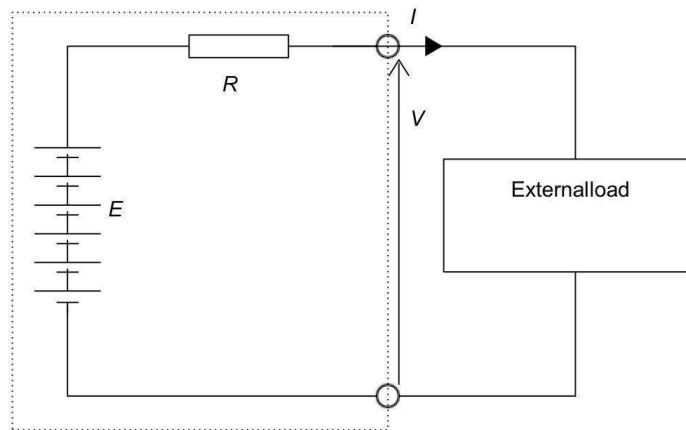


Figure 1.4 Simple equivalent circuit model of a battery [31]

The battery is made up of a maximum of six cells. It's worth noting that when the current I is zero, the voltage at the terminals rises to E , which is generally referred to as the open circuit voltage. When the battery is charged, the voltage rises by an entire break with respect to IR . To ensure flawless execution, it is necessary to reduce interior resistance in electric vehicle batteries.

1.2.2 Charge (or Amp-hour) capacity

The amount of electrical energy that a battery can provide is a critical characteristic. The standard unit for this measurement is the Coulomb, which represents the amount of charge while one Ampere runs for one second. The Coulomb, on the other hand, is far too tiny for practical use. Instead, an amp-hour (Ah) is a symbol indicating one Ampere running for one hour. The rating of a battery is commonly expressed in Amp-hours, for example, 10Ah. Therefore, the battery can deliver a current of 1 amp for 10 hours, 2 amps for 5 hours, or 10 amps for 1 hour hypothetically. In reality, however, most batteries do not operate exactly as expected. For example, a battery with an output of 42 Amp-hours is

indicated as $C = 42 \text{ Ah}$. Battery users frequently use phrases like "discharge rate of $2C$ " or "charging the battery at $0.4C$." In these cases, an expulsion current of 84 amps or an electrical charge of 16.8 amps is implied.

1.2.3 Energy stored

A battery's principal function is for saving energy. The level of voltage and charge of a battery define the amount of energy held within it. While the Joule is the SI unit for energy, its small magnitude makes it unsuitable for measuring battery energy. Instead, as a more handy unit, we often use the Watthour (Wh). The Watthour is equal to 3600 Joules and represents the electrical power a comparable to operating at one watt of power for a single hour. Using the Watthour corresponds to our use of the Amp-hour (Ah) for charging, resulting in a simple formula:

$$\text{Energy in Watthours} = \text{Voltage} \times \text{Amp-hours} \text{ or } \text{Energy} = V \times C \quad (1.2)$$

However, when using this equation, it is critical to use caution. It should be noted that the charge voltage (V) and, to a lesser extent, the Amp-hours capacity (C) can fluctuate significantly depending on how the battery is used. When the current is raised and a battery is rapidly depleted, both of these characteristics fall.

As a result, retained power becomes a fluctuating quantity that decreases as energy is swiftly released. It is common practice to quote stored energy in accordance with the Amp-hour rating, which means that if the charge potential is indicated for a five-hour discharge, the energy ought to naturally be provided for the same discharge frequency.

1.2.4 Energy capacity

Energy capacity refers to the quantity of electrical energy stored per kilogram of battery mass and is measured in units of Wh.kg^{-1} . By dividing the required energy capacity of the battery for a vehicle (in Wh) by the specific energy (in Wh.kg^{-1}), an initial estimation

of the battery mass can be obtained. However, it is important to note that the specific energy values provided are merely indicative, as the actual energy stored in a battery can significantly vary due to factors such as temperature and discharge rate.

1.2.5 Energy per unit volume

The quantity of electrical energy held per cubic meters of battery volume is referred to as energy per unit volume, and is commonly measured in Wh.m³. It is an essential metric since it allows us to calculate the battery's needed volume by dividing its energy capacity (in Wh) by its energy density (in Wh.m³). Alternatively, if we have a specified volume for batteries accessible, we can estimate the quantity of electrical energy that can be accommodated by multiplying the volume (in m³) by the energy density (in Wh.m³) of the battery. The volume of the battery can have a major impact on car design concerns. Energy capacity, like Energy per unit volume, is a notional value that provides an approximation.

1.3 LITHIUM-ION BATTERY

Individual lithium-ion cells are linked together in various configurations such as parallel (to raise current), series (to raise voltage), or a combination of both to form a lithium-ion battery. These cells are able to combine to form modules, which could then be combined to form a battery pack. As an example, the 85-kWh battery pack in a normal Tesla automobile is made up of 7104 cells. Each lithium-ion cell is typically made up of a cathode (positive electrode) and an anode (negative electrode) that are in interaction with an electrolyte, which is a fluid comprising lithium ions. A microporous polymeric membrane, which acts as a separator, separates the electrodes in a lithium-ion battery. This membrane allows lithium ions to pass between the electrodes while preventing electrons from flowing. In addition to the traditional liquid electrolyte, polymers, gels, and ceramics have been studied for use in lithium-ion batteries. Figure 1.4 depicts the basic operating principles of a standard lithium-ion battery unit.

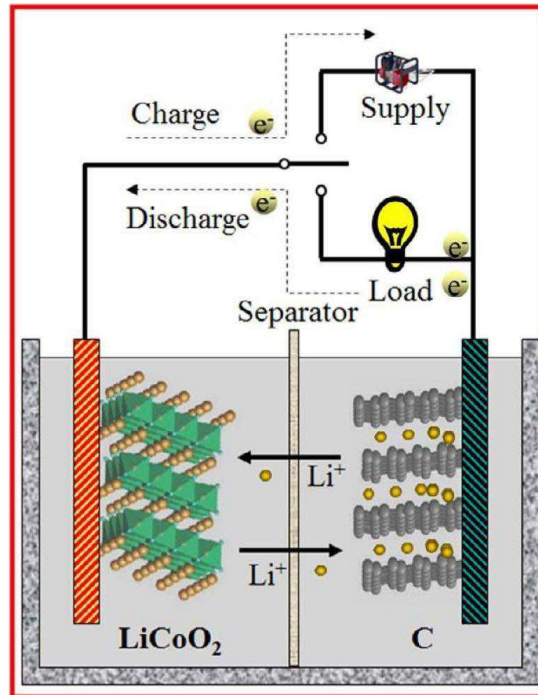


Figure 1.5 Illustration demonstrating the fundamental parts and workings of a Li-ion cell [29]

It is remarkable that, since Sony's first cells were commercialized two decades ago, the fundamental design of lithium-ion batteries has remained substantially constant. However, in-depth investigation has been made into various electrode materials, electrolytes, and separators in order to improve their functionality and properties.

1.4 BATTERIES IN FUTURE

A new era of sustainable transportation has begun with the growing popularity of electric vehicles (EVs), which responds to the pressing need to cut the release of greenhouse gases and minimize the environmental impact of conventional vehicles with combustion engines. The development of battery technology is essential to the success of electric vehicles (EVs), as batteries are the main means of energy storage and have a significant impact on the efficiency, range, and general viability of the vehicle.

Significant advancements in battery technology over the past several years have resulted in the creation of high-capacity, more dependable, and efficient battery systems designed

exclusively for electric vehicles. These innovations have completely changed the auto industry and have enormous potential for the development of electric mobility in the future. With an emphasis on the next opportunities and difficulties, this thesis attempts to investigate the new developments and trends in battery technology for electric cars.

1. *Lithium-ion Batteries (Li-ion)*: Due to their high energy density, lightweight construction, and extended cycle life, lithium-ion batteries are a particularly common type of battery used in electric vehicles. They deliver outstanding performance, dependability, and quick charging capacities. To store and release energy, lithium ions in Li-ion batteries move back and forth between the cathode and the anode.
2. *Lithium Iron Phosphate Batteries (LiFePO₄)*: Also known as LFP batteries, lithium iron phosphate batteries are a type of lithium-ion battery that utilizes iron phosphate as the cathode material. LiFePO₄ batteries offer enhanced safety, stability, and a longer lifespan compared to traditional Li-ion batteries. They are known for their thermal stability, high power density, and suitability for applications that prioritize safety.
3. *Nickel-Metal Hydride Batteries (NiMH)*: Hybrid electric vehicles (HEVs) and some early-generation electric cars have both made extensive use of nickel-metal hydride batteries. NiMH batteries have advantages in terms of reduced cost, longer cycle life, and greater tolerance to high temperatures, but having a density of energy that is less than lithium-ion batteries. However, due to lithium-ion technology's dominance, their use in contemporary electric vehicles has decreased.
4. *Solid-State Batteries*: A new technology that holds considerable potential for the development of electric cars is solid-state batteries. These batteries offer benefits including higher energy density, greater security, quicker charging, and longer lifespan by swapping out the

liquid electrolyte used in conventional batteries for a solid electrolyte. Although they are still in the research and development stage, solid-state batteries have the potential to completely transform the electric car market.

5. *Zinc-Air Batteries:* Airborne oxygen serves as the reactant in zinc-air batteries, which use it to produce power. They are ideal for applications involving electric vehicles due to their high energy density and minimal weight. However, because zinc-air batteries often need to be replaced when they run out of power, they are limited in terms of their ability to be recharged.

It's crucial to remember that the selection of battery for electric vehicles depends on a number of variables, including price, energy density, power needs, weight concerns, and the unique requirements of the vehicle. To enhance the energy storage capacity, charging efficiency, and general performance of electric vehicles, the industry is constantly studying and developing new battery technologies.

1.5 OBJECTIVES OF THESIS

The thesis work examines the performance of a unique liquid cooling design based on small channel cold plates dispersed along the height of the cells and cooled by water. A three-dimensional Computer-aided design (CAD) model was created for the proposed design using Ansys Space Claim, and numerical simulations were run using the CFD solver in the software Ansys Fluent to solve the continuity equation, Navier-Stokes equation, and Energy equation. The specific objectives of the thesis can be summarised as:

- i. To examine the maximum temperature of the battery pack for 3C and 4C discharge rate under varying flow rate/ Reynolds number
- ii. To examine the fluid outlet temperature for 3C & 4c discharge rate under varying Reynolds number.

- iii. To examine the pressure-change between the intake & the exit of the mini channel of cooling plate for 3C & 4C discharge rate under varying Reynolds number.
- iv. Finally, to investigate the minimum possible peak temperature of cell, maximum pressure difference and maximum fluid outlet temperature at highest Reynolds number such that the flow is still laminar.

CHAPTER 2

LITERATURE REVIEW

Skerlos and Winebrake [1] looked into the societal advantages of plug-in hybrid electric and other forms of electric automobiles that could improve our environment, wellness, and sustainability of energy. To address environmental pollution and decrease reliance on fossil fuels, the automotive industry is increasingly emphasizing the use of sustainable energy sources. The transition from conventional fossil fuel-powered vehicles to electric vehicles is a significant stride in this direction. The increasing adoption of electric vehicles (EVs) has presented a range of difficulties concerning the power storage elements. Zhao et al. [2] evaluate the effectiveness of the serpentine channel system of cooling using thermal modelling simulation. Lithium-ion batteries (LIBs) have appeared as favourable choices for power storage in EVs due to their desirable characteristics, including high energy content/volume, minimal auto-discharge rate, and extended lifespan. Spotnitz and Franklin [3] simulate abusive evaluation of lithium-ion cells in order to examine the thermal runaway phenomenon. The operational temperature range and uniformity of temperature across cells play crucial roles in determining various aspects of battery module performance. The temperature directly influences the rate of exothermic chemical reactions, which significantly impacts battery performance. Bandhauer et al. [4] suggested thermal management strategies for lithium-ion batteries. Within a temperature between of 20 & 40 °C, lithium-ion batteries provide the best performance. Amid the charging and releasing forms, a significant sum of warm is created, driving to the plausibility of overheating or indeed combustion of lithium-ion batteries. In addition to overheating, the lack of uniform heat distribution among individual cells is a significant issue that requires attention. The inconsistent heat distribution greatly limits how well the battery pack performs, as it can lead to the failure of certain cells and result in a substantial voltage drop across the pack [5]. Li et al. [6] explored improvement for fluid cooling cylindrical battery thermal management system. It's critical to reduce the temperature variance between individual cells. Greco et al. [7] carried out a mathematical and numerical study on the thermal management of lithium-ion battery cells in battery-powered cars using thermal pipes. Therefore, maintaining the

reliability and effectiveness of the battery thermal management system (BTMS) is crucial for preserving the security of electric vehicle.

Li et al. [8-9] examine the low temperature conduct of lithium particle batteries. According on the cooling method used, BTMSs can be classified as using cooling by liquid, air cooling, phase change material (PCM), or mixtures of these. Kim et al. [10-11] suggested a unique battery thermal management system to provide an efficient thermal management approach for lithium-ion cells with a significant amount of energy. Air cooling involves utilizing a fan to blow air through the module. However, because air has a limited thermal conductivity, its effectiveness is reduced in situations involving high discharge rates and hot environments. PCM cooling, on the other hand, utilizes the Solid-liquid phase shift of phase change materials to mitigate thermal non-uniformities within the battery module. Wei et al. [15] investigated a simple capillary-based air conditioning channel for battery temperature control. While the PCM cooling system exhibits remarkable cooling performance, it is important to consider the associated drawbacks such as its high cost, heavy weight, encapsulation and volume change limits its application. Heat pipe cooling, although effective, requires additional cooling methods to complete the condensation section, resulting in increased costs. In comparison, liquid cooling is a widely applied solution in Battery heat management system due to its versatility and extensive range of applications.

Liquid cooling has gained widespread adoption in electric vehicles (EVs) due to several reasons. Hallaj et al. [17] employ phase-change material (PCM) in their innovative battery temperature management system. Firstly, liquids offer superior thermal performance in terms of thermal capacity and heat conductivity compared to air. Second, compared to PCM systems for cooling, liquid-cooled systems have a more compact construction and are less expensive. Finally, compared to heated pipe cooling methods, liquid-cooled systems are seen to be more dependable. Using various coolant temperatures and discharge rates, Malik et al. conducted research on the cooling efficiency of the battery thermal management system (BTMS) [18]. They concentrated on analyzing how coolant temperature [19] and the surrounding temperature [23] affected the performance of the BTMS for battery modules that were linked in series. To get the best cooling efficiency, Al-Zareer et al. [20] emphasized the need of using coolants with high thermal conductivity. Wang et al. investigated the impact of coolant flow velocity

and individual cell configuration (serial and parallel) on BTMS performance. They found that raising the coolant flow rate improved the cooling efficiency and that the concurrent cooling architecture improved temperature distribution uniformity. Hong et al. [21] promoted a two-phase coolant as the best coolant for use in conventional liquid-cooled systems.

Lai et al. [22] focused on making liquid cooling systems small and compact. While extensive literature exists on liquid cooling, only a limited number of researchers have specifically analyzed liquid cooling for cylindrical cells. Zhao et al. [23] introduced a novel liquid cooling technique called Compact Liquid Cooled Cylinder (LCC) and analyzed the effects of various operating parameters. Their findings revealed that maintaining a maximum temperature below 40°C was achievable by using four channels and a mass flow rate of 10-3 kg/s. Additionally, when the number of channels was greater than eight, LCC cooling outperformed natural convection cooling. Rao et al. [24] employed aluminum blocks with varying contact surface areas to develop a liquid cooling-based Battery Thermal Management System (BTMS) for cylindrical lithium-ion battery modules. Their study focused on a battery module with six cells in the flow direction and observed that adjusting the contact surface area of the aluminum block along the flow direction improved temperature uniformity. The optimal design was determined by considering factors such as parasitic power, BTMS weight, and thermal efficiency. Pakrouh et al. [25] set out to create a trade-off between cooling effectiveness and system pressure reduction. They looked at discharge rate (3C and 5C), slurry content of Microencapsulated Phase Change Material (10% and 20%), and fluid velocity (up to 0.4 m/s). Zhao et al. [26] investigated the impacts of discharge/charge C-rate, fluid flow rate, heat transfer surface between nearby battery packs, and battery proximity with the channel's outer layer. Based on a half-helical duct, Zhou et al. [27] suggested a liquid-cooled BTMS for cylindrical cells. They studied the effects of design parameters such as inlet mass transfer rate, direction of flow, pitch and number of helical vents, and vent size using computational fluid dynamics (CFD). The effect of pitch and the number of helical vents was unclear, however changes in flow direction were shown to significantly improve thermal performance. Furthermore, as duct diameter increased, maximum temperatures increased and temperature disparities decreased.

Huang et al. [28] investigated the impact of temperature interaction and dispersion of heat of cylindrical Lithium-Ion cells. Despite the substantial quantity of research on cooling by liquids of lithium-ion batteries, the majority of proposed designs center on prismatic-shaped cells. Furthermore, existing research on liquid cooling for cylindrical cells focuses on the effects of parameters such as the rate of flow, direction of flow, and duct number. To the best of our knowledge, no previous research has looked into the effects of cooling surface and small channel architecture, flow features, and battery layout. Saw et al. [29] performed a Numerical analysis and thermal investigation of a lithium-ion rechargeable battery with cooling by air. To address this research gap, the present study introduces an innovative liquid cooling design utilizing mini channel cold plates distributed vertically along the height of the cells, with water serving as the cooling medium. A three-dimensional computer-aided design (CAD) model was developed to represent the proposed design. Bernadi et al. [30] was incorporate methodology to understand the heat dissipation model and evaluate the thermodynamic energy balance of lithium-ion batteries. For discharge rates of 3C and 4C, computational fluid dynamics (CFD) computations were run on the battery pack to examine the impacts of the highest temperature, maximum temperature variation within the pack, and liquid pressure reduction.

CHAPTER 3

METHODOLOGY & MODEL DESCRIPTION

Several critical steps are involved in the numerical methodology used to explore the assessment of the suggested liquid cooling system and its impact on temperature regulation and overall performance. First, a 3-D CAD design for the battery pack is created, which includes the small channel cold plates and battery cells. The CAD model is then discretized to create a computational mesh. Limiting conditions are applied to the walls of the battery pack and mini channel cold plates, followed by CFD-solver repeatedly solving the discretized equations governing them and CFD-post interpreting to visualize variables like the highest temperature within the cells, temperature distribution, temperature differences, and pressure drop. Section 3.1 of Chapter 3 discusses the necessary Problem statement and Heat dissipation model to analyse the thermodynamic energy balance of lithium-ion batteries. Furthermore, in section 3.2, assumptions, fundamental partial differential formulations that are continuous, such as the Navier-Stokes Energy equation for coolant flow, battery, and cold plate are briefly examined. Section 3.2.3 also goes into detail on the critical boundaries and schemes employed in the CFD solution. Section 3.3 discusses the mesh formation phenomenon as well as grid sensitivity evaluation, which compares the results based on the size of the grid utilized in the fluid flow domain. Finally, section 3.4 presents the confirmation of the computational approach used in this thesis.

3.1 PROBLEM STATEMENT AND GEOMETRY OF BATTERY PACK WITH MINI CHANNEL

The study considers a cylindrical lithium-ion battery pack (4 rows in series, each row with 10 cells parallelly coupled) positioned inline. A water cooling BTMS for cylindrical 18,650 cells with 6 U-form channels dispersed along the length of the cell was set up in the present study, as demonstrated in Fig. 3.1. The front perspective of the design is depicted in Fig. 3.2. Each module is composed of a total of 40 cells. Table 3.1 depicts the

geometric design of the U-formed channel. d is a fixed value of half a millimeter, the cooling plate height is 65 mm. The width of the cooling plate is denoted by t , which is (mm). The cooling plate wall depth is denoted by t_w (mm). The intake coolant is chosen to be water, while T_c (K) represents the temperature of the inflow fluid. The inflow water velocity is denoted by u (m/s).

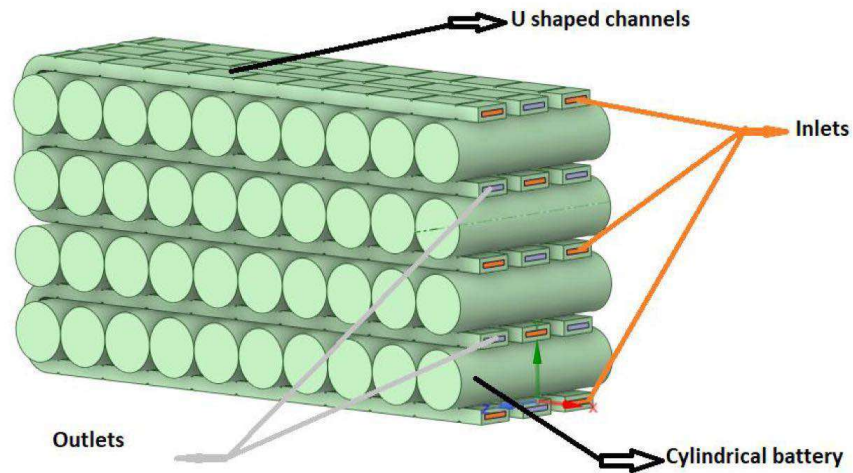


Fig. 3.1 3D view of U-shaped channels with battery pack

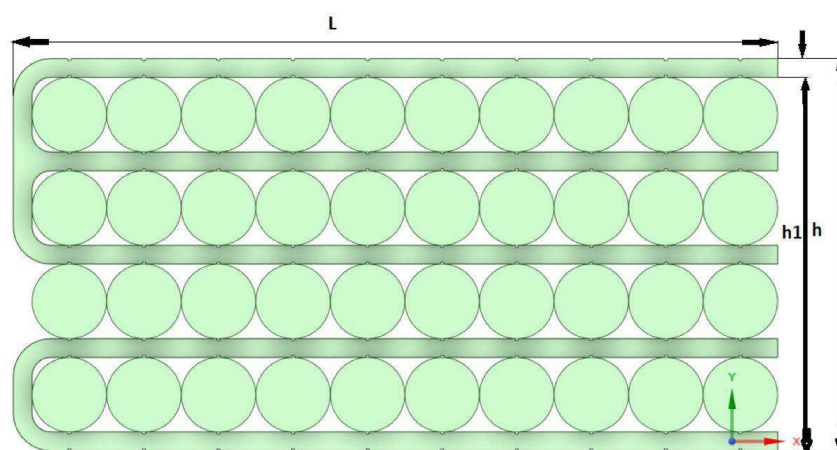


Fig. 3.2 Front view of geometry along with dimension

Table 3.1 Value of U-shaped channel geometric parameters

| | |
|----|-------------|
| t1 | 5.1 |
| t2 | 1.48 |
| h | 64 |
| H1 | 63 |
| L | 199 mm + t1 |
| D1 | 1.5 mm |
| d | 0.5 mm |

The research focuses on the 18650-model cylindrical lithium-ion battery, which has an 18 mm diameter and a 64 mm height. Previous literature [28] was used to acquire the heat generation model, size, and thermophysical parameters of the cells. To simplify the computations, the thermophysical parameters of the cells are considered to be uniform and independent of operating time and temperature. Table 3.2 shows the particular values of these thermophysical characteristics. Aluminum is used for both the cooling plates and the battery housing due to its advantages of superior thermal conductivity and low density. Water was chosen as the coolant medium due of its high heat capacity and low cost.

Table 3.2 Thermophysical properties of Lithium-ion cell [28]

| Parameters | Value | |
|--------------------------|---------------------------------------|-------------|
| Rated voltage | 3.2 V | |
| Rated capacity | 1.35 Ah | |
| Equivalent density | 2018 kg/m ³ | |
| Equivalent specific heat | 1282 J/(kg·K) | |
| Volume (V) | 1.654×10 ⁻⁵ m ³ | |
| Thermal conductivity | Radial Direction | 0.9 W/(m·K) |
| | Axial Direction | 2.7 W/(m·K) |
| Length | 65 mm | |

The material properties of aluminum and water, as given in Table 3.3, are also assumed to be uniform and constant over time and varying temperature.

Table 3.3 Material properties of aluminium and coolant

| Material | Density (kg/m^3) | Specific heat capacity ($\text{J}/\text{kg}\cdot\text{K}$) | Thermal conductivity ($\text{W}/\text{m}\cdot\text{K}$) | Viscosity($\text{kg}/\text{m}\cdot\text{s}$) |
|----------|---------------------------------------|--|---|--|
| Aluminum | 2719 | 871 | 202.4 | N/A |
| Water | 998.2 | 4182 | 0.6 | 0.000798 |

The analysis excludes the thermal contact resistance between the cooling plate and the cells, which is caused by the unevenness of the battery surface and the contact area between the cooling plate and the cells. In real-world applications, however, this contact thermal resistance can be reduced by putting thermal lubricant at the interface. Thermal contact resistance between the cooling plate and cells must be considered since it is impacted by surface unevenness and differences in the contact area. This factor has a substantial impact on the system's overall thermal performance. However, the thermal contact resistance between the cooling plate and the cells, including the contact area, is not considered in this study. Contact thermal resistance could be lowered in practical applications.

3.2 NUMERICAL FORMULATION AND BOUNDARY CONDITIONS

3.2.1 Heat dissipation model

Bernadi et al. [29] evaluated the thermodynamic energy balance of lithium-ion batteries in their study. They assumed a uniform distribution of cell temperature and attributed the temporal variation of cell temperature to numerous elements such as changes, variations in the system's thermal capacity, changes in phase, combining, power and heat exchange with the outside environment. They developed a simpler formula for the thermal energy release rate during discharge in a lithium-ion battery by excluding the heat created by mixing and phase transitions. For their analysis, this equation functioned as a simplified

form.

$$Q = \left(I^2 R + IT \frac{\partial E_o}{\partial T} \right) / V_b \quad (3.1)$$

Q represents the thermal energy generation rate, I represent the drain current, R represents the ohmic resistance within the cells, EO represents the open circuit voltage, T represents the cell temperature, EO/T represents the entropy weight coefficient, and V_b represents the battery volume. Simulations utilizing the Bernadi equation, as previously described in the research, were used to determine volumetric heat generation values for various discharge rates. Table 3.4 contains these values. The discharge process takes place at a constant current, and the discharge rate is measured in C rate, which indicates how quickly the cell is discharged in comparison to its maximum capacity. For example, with a 10 A-h battery, a drain at 1C rate equals to a drain current of 10 A.

Table 3.4 Volumetric Heat energy generation for various discharge rates

| Discharge rate | Discharge current | Internal resistance | $\frac{dEO}{dT}$ | Volume | Volumetric heat generation |
|----------------|-------------------|---------------------|------------------|------------------------------------|----------------------------|
| 1 C | 1.35 A | 40 mΩ | 0.01116 V | $1.645 \times 10^{-5} \text{ m}^3$ | 5318 W/m ³ |
| 2 C | 2.70 A | 40 mΩ | 0.01116 V | $1.645 \times 10^{-5} \text{ m}^3$ | 19452 W/ m ³ |
| 3 C | 4.04 A | 40 mΩ | 0.01116 V | $1.645 \times 10^{-5} \text{ m}^3$ | 42400 W/ m ³ |
| 4 C | 5.38 A | 40 mΩ | 0.01116 V | $1.645 \times 10^{-5} \text{ m}^3$ | 74163 W/ m ³ |

During the discharge process, the heat created by the cells is transmitted to the aluminium cooling plate by thermal conduction and subsequently released into the surrounding air via natural convection. The cooling plate receives heat from the cells, which is subsequently removed by the liquid coolant through forced convection. Additionally, the aluminium casing that is in contact with the cooling plates also contributes to heat dissipation through natural convection. Although there is a small amount of heat removal

through radiative heat transfer from all surfaces, it is negligible within the cell's operating temperature range of 300 to 320 K and is therefore not considered in this study.

3.3 ASSUMPTIONS AND BOUNDARY CONDITIONS

3.3.1 Assumptions

An analytical model was developed to simplify the calculations, relying on certain assumptions. The fluid flow was supposed to have reached a steady state, and material thermophysical parameters such as thermal conductance and thermal capacitance were assumed to be uniform and temperature independent. The greatest velocity of the coolant utilised in the study was 0.64 m/s, which is much less than the velocity of sound when water is assumed to be incompressible. The Reynolds number, a dimensionless parameter that compares inertial and viscous forces in the fluid, was used to predict the flow regime. The Reynolds number corresponding to the maximum velocity employed in this research is

$$R_e = \frac{\rho v D}{\mu} = \frac{998.2 \times 0.26 \times 2.6 \times 10^{-3}}{0.000798} = 845.59 \quad (3.1)$$

When the Reynolds number is lower below 2300, the flow is in the laminar domain. The cells' thermal conductance is believed to be bidirectional. Furthermore, gravity's influence is ignored in the analysis. Furthermore, because of the working temperature range of 300 to 320 K, the transfer of radiation is ignored.

3.3.2 Governing Equation

The coolant medium used in the system liquid water, characterized through its density (ρ_w), specific heat capacity (CP_w), temperature (T_w), velocity (v^{\rightarrow}), dynamic viscosity (μ_w), pressure (P_w), and thermal conductivity (kw). The energy conservation equation [30] describes the thermal behaviour of the coolant as it flows through the mini channel.

$$\frac{\partial(\rho_w C_{pw} T_w)}{\partial T} + \nabla \cdot (\rho_w C_{pw} T_w \vec{v}) = \nabla \cdot (k_w \nabla T_w) \quad (3.2)$$

The continuity equation for the flow of coolant is given by [30].

$$\frac{\partial \rho_w}{\partial T} = \nabla \cdot (\rho_w \vec{v}) = 0 \quad (3.3)$$

The simplified expression can be obtained by considering the assumption of incompressibility ($\partial \rho_w / \partial t = 0$).

$$\nabla \cdot (\vec{v}) = 0 \quad (3.4)$$

The equation governing the momentum of the coolant flow is expressed as [31].

$$\rho_w \left[\frac{\partial \vec{v}}{\partial t} + (v \cdot \nabla) v \right] = -\nabla P_w + \mu_w \nabla^2 v \quad (3.5)$$

Additionally, the energy conservation equations for the battery and cooling plates can be represented as [32].

$$\rho_B C_B \frac{\partial T_B}{\partial t} = \left(k_{Bx} \frac{\partial^2 T_B}{\partial x^2} + k_{By} \frac{\partial^2 T_B}{\partial y^2} + k_{Bz} \frac{\partial^2 T_B}{\partial z^2} \right) + Q \quad (3.6)$$

$$\rho_A C_A \frac{\partial T_A}{\partial t} = k_A \left(\frac{\partial^2 T_A}{\partial x^2} + \frac{\partial^2 T_A}{\partial y^2} + \frac{\partial^2 T_A}{\partial z^2} \right) + v(\rho_A C_A \nabla T_A) \quad (3.7)$$

Subscript A represents aluminium and B represents the battery. In the equations, ρ_A , C_A , T_A , and k_A denote the mass density, heat capacity, temperature, and thermal conductivity of the aluminium, respectively, while v represents the velocity of the coolant.

3.3.3 Boundary Conditions

The individual battery has a rated voltage and a rated current capacity mentioned previously. The cooling channel is constructed from aluminium, while the fluid used is water. The heating characteristics of the Battery Thermal Management System are presented in below. Heat source density (Q) for various discharge rates can be found in Table 3. The rate of discharge is set to 3C and 4C for the present study, resulting in volumetric heat generation rates of 42,400 W/m³ and 74,613 W/m³ correspondingly. The heat transfer factor (h) of the system's exterior surfaces is 5 W/(m²K). The temperature outside (T_0) is defined as 298.15 K. The outlet boundary criteria is a pressure outlet with a gauge pressure of 0 Pa, while the inlet boundary condition is a velocity inflow. The fluid flow is deemed to be in the category of laminar flow because the Reynolds number is lower than 2300.

CHAPTER 4

VALIDATION AND GRID INDEPENDENCE TEST

4.1 VALIDATION

In this computational study, the validation of the 6 staggered U form mini channel cooling plate for lithium ion cell module is conducted. The obtained results are then used to create plots representing the maximum temperature difference rise with input velocity of fluid in the six U form channel design for evaluation with the actual results is shown in. Fig. 4.1 The validation process involved testing at 3C drains rate.

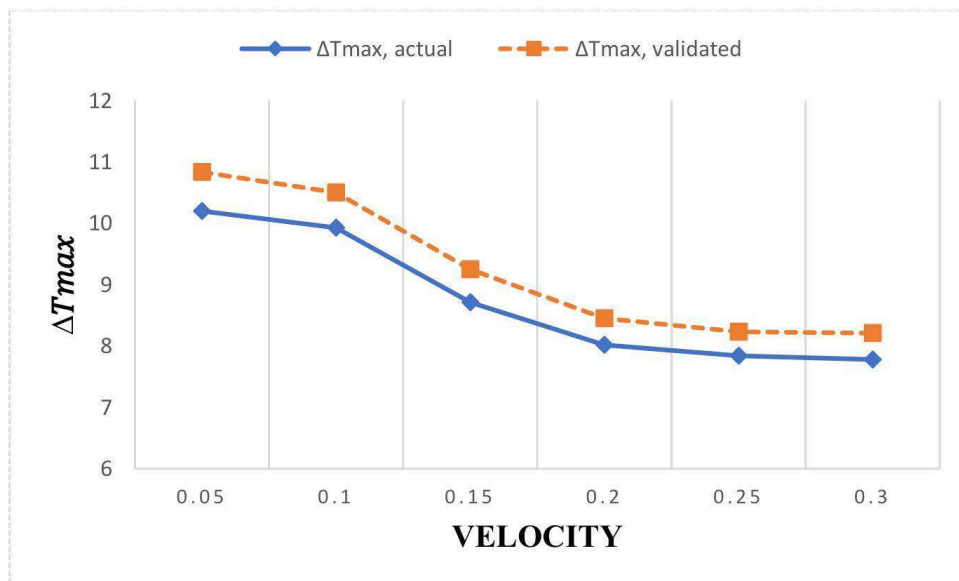


Fig. 4.1 Variation of change in maximum temperature difference of actual and validated results with increase in velocity

Table 4.1 displays the variation in the maximum temperature difference between the actual and validated results of the cell surface temperature as velocity increases, calculating the percentage inaccuracy.

Table 4.1 Variation ΔT_{\max} , actual & ΔT_{\max} , validated with velocity to calculate % Error

| S.NO | Velocity | ΔT_{\max} , actual (K) | ΔT_{\max} , validated (K) | % Error |
|------|----------|-----------------------------------|--------------------------------------|---------|
| 1 | 0.05 | 10.2 | 10.834 | 6.21% |
| 2 | 0.1 | 9.93 | 10.5 | 5.80% |
| 3 | 0.15 | 8.71 | 9.25 | 6.23% |
| 4 | 0.2 | 8.02 | 8.453 | 5.40% |
| 5 | 0.25 | 7.84 | 8.23 | 5.10% |
| 6 | 0.3 | 7.78 | 8.21 | 5.60% |

- Numerical arrangements are went with by different sorts of flaw making the arrangements far-fetched on its precision.
- As a result, approval of the computational outcomes obtained is required using the test data or with the existing dispersed investigation data.
- In this ponder the results were approved with actual results inquire about where the maximum fallacy within the result was found to be 6.21 % and minimum error was 5.10 %.

4.2 MESH GENERATION AND GRID INDEPENDENCE TEST

Mesh is an important feature of modelling using CFD since it discretises the geometry into basic elements that can be used as distinct nearest approximations of the computational field. A polyhedral mesh with 4 million elements is shown in Fig. 4.2 Polyhedral mesh is chosen because, in comparison to other meshes, it has a quicker convergence rate with a smaller number iterations, resilient convergence for lower values of residuals, and more rapid result runtimes.

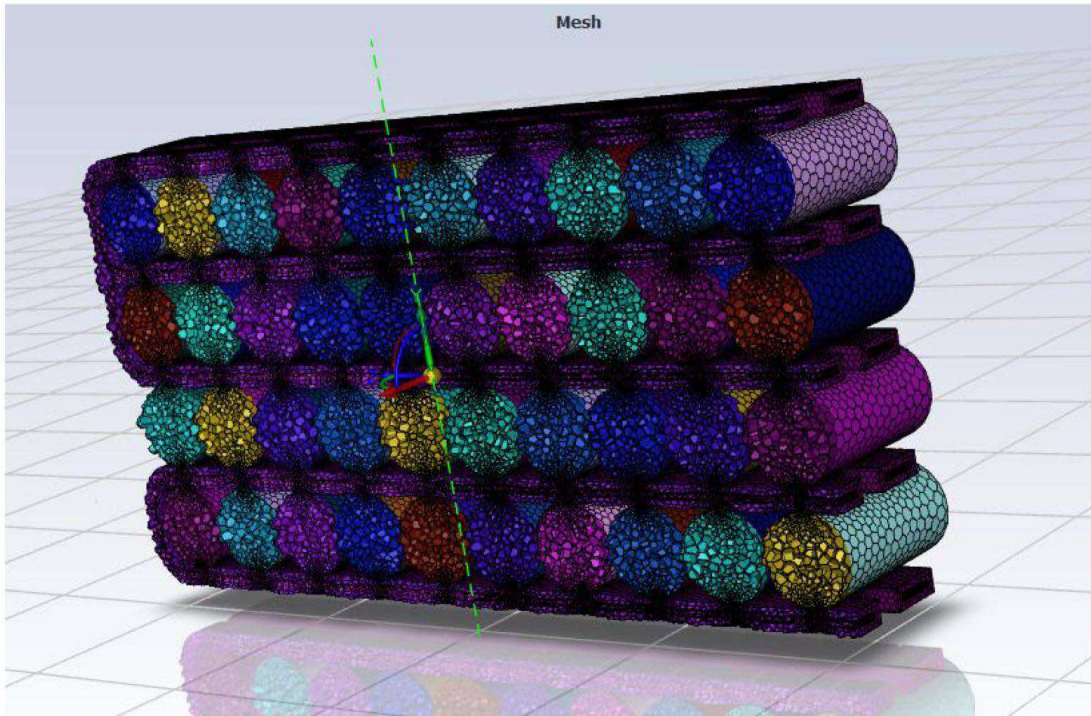


Fig. 4.2 Polyhedral mesh with 4 million elements

Figure 4.3 depicts the fluctuation of maximum temperature with node count. The solution variables weren't modified much after a mesh of 4835020 node points, consequently this value could be used for subsequent calculations

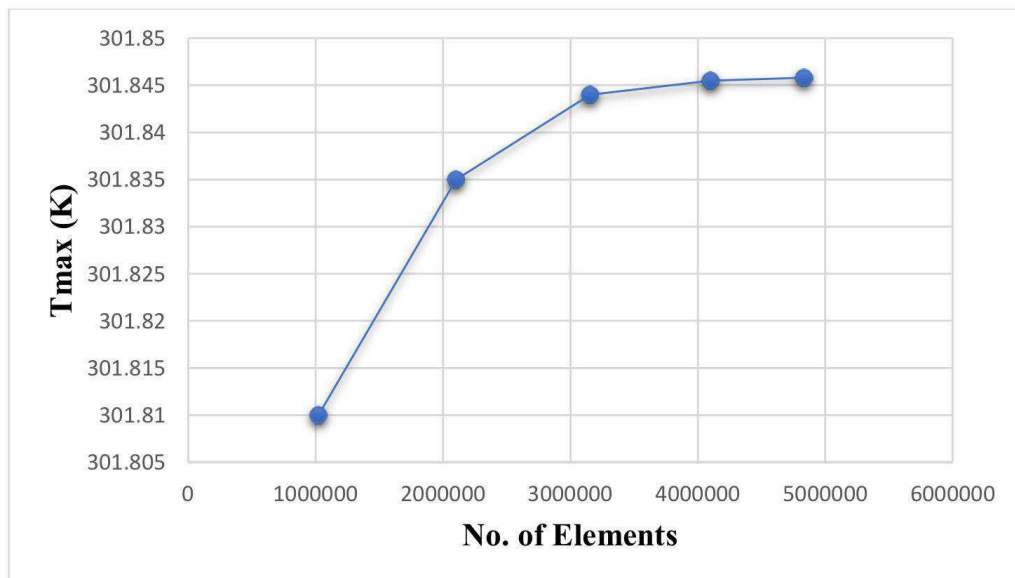


Fig. 4.3 Grid independence test

CHAPTER 5

RESULTS & DISCUSSION

5.1 RESULTS OF MAXIMUM TEMPERATURE, PRESSURE DROP AND FLUID OUTLET TEMP OF BATTERY PACK FOR 3C DISCHARGE RATE UNDER VARYING REYNOLDS NUMBER

Under 3 C drain rate Table 5.1 shows the fluctuation in T_{max} , ΔP and $T_{c,out}$ with increasing R_e for the following constant parameters:

- Mesh size: Polyhedral mesh with no. of elements is 48,35,020.
- Volumetric heat generation is 42400 W/m^3
- Ambient temperature is same as fluid inlet temperature = 298.15 K

TABLE 5.1 Variation of T_{max} , ΔP and $T_{c,out}$ with R_e for 3C

| R_e | T_{max} (K) | ΔP (Pa) | $T_{c,out}$ (K) |
|-------|---------------|-----------------|-----------------|
| 900 | 301.689 | 492 | 345.517 |
| 1200 | 300.727 | 646.76 | 346.944 |
| 1500 | 300.978 | 957.2048 | 347.161 |
| 1800 | 300.177 | 14166.67 | 348.296 |
| 2100 | 300.183 | 2096.65 | 348.518 |

Fig. 5.1 (a) shows the temperature distribution of cell surface temperature for $R_e = 900$ & Fig. 5.1 (b) shows the temperature distribution of cell surface temperature for $R_e = 1200$. Subsequently, Fig. 5.1 (c) shows the temperature distribution of cell surface temperature for $R_e = 1500$, Fig. 5.1 (d) shows the temperature distribution of cell surface temperature for $R_e = 1800$ & Fig. 5.1 (e) shows the temperature distribution of cell surface temperature for $R_e = 2100$

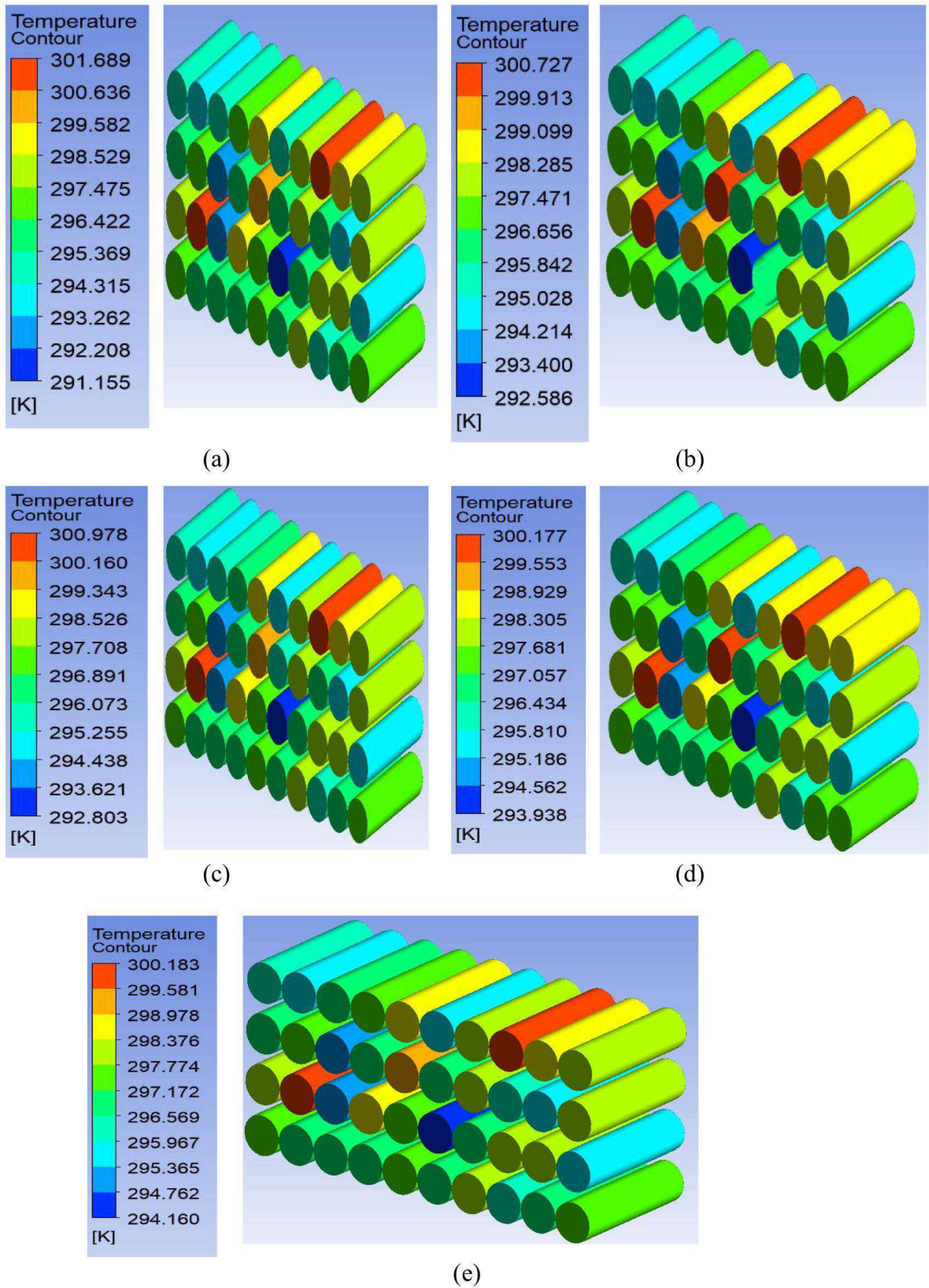


Fig. 5.1 Temperature contours of cells during 3C drain rate for (a) $R_e = 900$, (b) $R_e = 1200$, (c) $R_e = 1500$, (d) $R_e = 1800$, (e) $R_e = 2100$

It is clear from Figure 5.1 (a) that the two cells out of 40 cell pack have reached the maximum temperature to 301.689 K during 3C drain rate for Reynolds number of 900.

As the Reynolds number is increased by 300, Figure 5.1 (b) shows that the three cells have reached maximum temperature to 300.177 K for Reynolds number of 1200.

From Figure 5.1 (c) it can be visualised that however the maximum cell temperature has reached to 300.978 K but the average temperature of 40 cells have reduced for Reynolds number of 1500

Figure 5.1 (d), clearly depicts that the three cells have reached maximum temperature of 300.177 K for Reynolds number of 1800

Figure 5.1 (e) shows that the maximum temperature of cells has reached to 300.183 and there is very little change in the maximum temperature as we increase Reynolds number further.

5.1.1 Parametric study of Result of Maximum Temperature (T_{max}) for 3C drain rate

As the Reynolds number increases, the maximum temperature decreases. Furthermore, the most extreme temperature rises noticeably as coolant outlet temperature (T_c) rises, correlating with previous affectability research findings. As a result, it is recommended to prioritize reducing the cooling fluid temperature at the entry of air and increasing the speed of the incoming coolant flow in order to increase the heat dissipation effectiveness of the Battery thermal management. Simultaneously, lowering the thickness of the cooling plate wall can improve the system's total cooling efficiency. For $Re=2100$, the lowest maximum temperature is 300.183K.

Fig. 5.2 (a) shows the pressure distribution of fluid channel for $R_e = 900$ & Fig. 5.1 (b) shows the pressure distribution of fluid channel for $R_e = 1200$. Subsequently, Fig. 5.1 (c) shows the pressure distribution of fluid channel for $R_e = 1500$, Fig. 5.1 (d) shows the pressure distribution of fluid channel for $R_e = 1800$ & Fig. 5.1 (e) pressure distribution of fluid channel for $R_e = 2100$

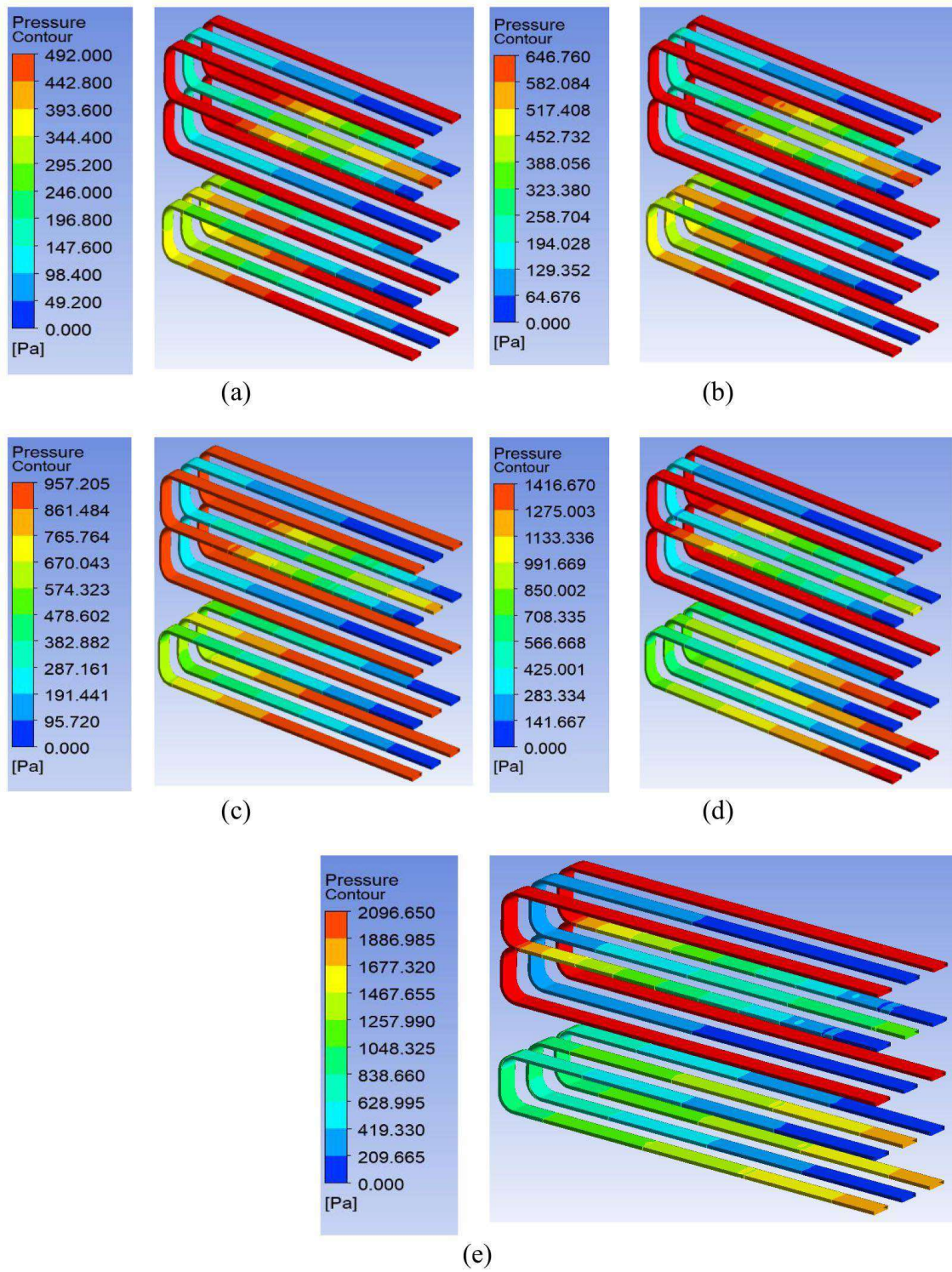


Fig. 5.2 Pressure drop of fluid channel during 3C drain rate for (a) $R_e = 900$, (b) $R_e = 1200$, (c) $R_e = 1500$, (d) $R_e = 1800$, (e) $R_e = 2100$

It is clear from Figure 5.2 (a) that the pressure is maximum at inlet sections and the maximum pressure reached is 492 Pa during 3C drain rate for Reynolds number of 900. Here it is also additionally visualised that at the bend sections the pressure is more due to added component of bend friction losses.

As the Reynolds number is increased by 300, Figure 5.2 (b) shows that the maximum pressure reached has increased to 646.76 Pa for Reynolds number of 1200.

From Figure 5.2 (c) it can be visualised that however the maximum pressure has reached to 957.205 Pa but at the front inlet sections the pressure is reduced for Reynolds number of 1500.

Figure 5.2 (d), clearly depicts that maximum pressure has increased up to 1416.67 Pa for Reynolds number of 1800.

Figure 5.2 (e) shows that however the maximum pressure has increased to 2096.65 Pa but at the front intake sections the pressure is decreased for Reynolds number of 2100.

5.1.2 Parametric study of Result of Pressure Drop (ΔP) for 3C

- As we can observe from the pressure contours that as the flow rate is increased at higher Reynolds no.
- The pressure drop is increased due to increase in the velocity and flow rate of fluid i.e., water in this case. For 3C discharge rate the maximum pressure is at higher Reynolds no. = 2100 which is equal to 2096 Pa.
- Furthermore, the pressure drop is a function of friction factor and hence we can conclude that the increased flow rate and velocity of fluid increases the friction in the fluid channel which further increases the pressure drop.
- Additionally, the increased pressure drop increases the pumping power required for the fluid or coolant which additionally increases the cost.
- Additionally, we can observe that the maximum pressure drop is observed at the intake sections.

5.1.3 Parametric study of fluid outlet temperature ($T_{c,out}$)

- As watched from the comes about that the Liquid outlet Temperature is expanded on expanding the stream rate and at the next Reynolds no.
- On expanding the Reynolds No., the warm scattering from the surface to the fluid channel through conduction and after that convection mode of warm exchange increments and thus the liquid outlet temperature is expanded.
- For 3C release rate the greatest liquid outlet temperature is watched is 348.518K at $Re = 2100$ for 3C deplete rate.

5.2 RESULTS OF MAXIMUM TEMPERATURE, PRESSURE DROP AND FLUID OUTLET TEMP OF BATTERY PACK FOR 4C DISCHARGE RATE UNDER VARYING REYNOLDS NUMBER

Under 4 C drain rate Table 5.2 shows the fluctuation in T_{max} , ΔP and $T_{c,out}$ with increasing Re for the following constant parameters:

- Mesh size: Polyhedral mesh with no. of elements is 48,35,020.
- Volumetric heat generation is $74163 W/m^3$
- Ambient temperature is same as fluid inlet temperature = 298.15 K

TABLE 5.2 Variation of T_{max} , ΔP and $T_{c,out}$ with Re for 4C

| Re | T_{max} (K) | ΔP (Pa) | $T_{c,out}$ (K) |
|------|---------------|-----------------|-----------------|
| 900 | 302.419 | 437 | 384.40 |
| 1200 | 302.1489 | 646.76 | 384.62 |
| 1500 | 302.047 | 957.205 | 385.04 |
| 1800 | 301.83 | 1416.66 | 385.08 |
| 2100 | 301.89 | 2096.65 | 384.96 |

Fig. 5.3 (a) shows the temperature distribution of cell surface temperature for $Re = 900$ & Fig. 5.3 (b) shows the temperature distribution of cell surface temperature for $Re = 1200$. Subsequently, Fig. 5.3 (c) shows the temperature distribution of cell surface temperature for $Re = 1500$, Fig. 5.3 (d) shows the temperature distribution of cell surface temperature for $Re = 1800$ & Fig. 5.3 (e) shows the temperature distribution of cell surface temperature for $Re = 2100$.

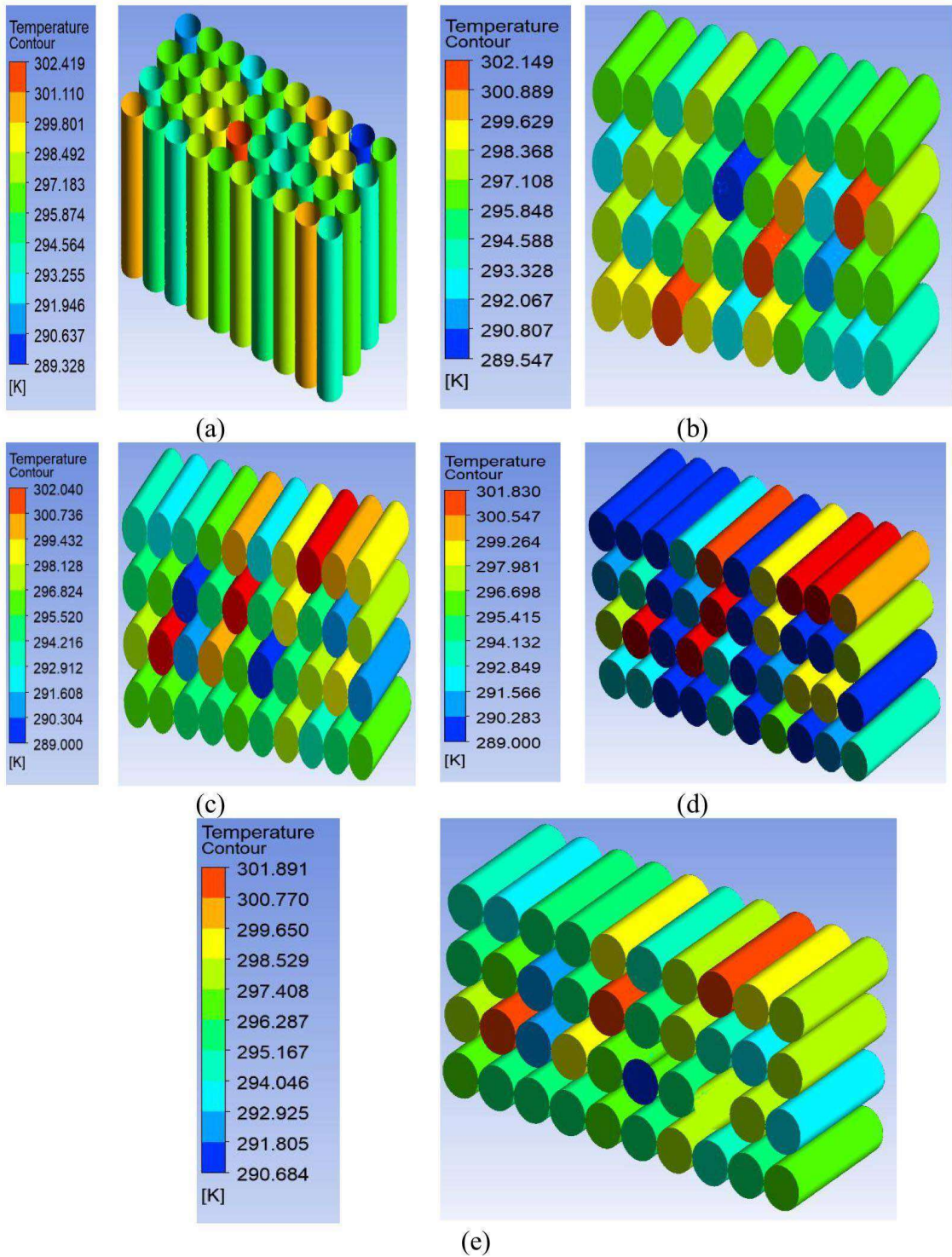


Fig. 5.3 Temperature contours of cells during 4C drain rate for (a) $R_e= 900$, (b) $R_e= 1200$, (c) $R_e=1500$, (d) $R_e=1800$, (e) $R_e= 2100$

Figure 5.3 (a) shows that two cells out of a 40-cell pack reached the maximum temperature of 302.419 K at a 3C drain rate with a Reynolds number of 900.

Figure 5.3 (b) illustrates that as the Reynolds number increases by 300, the three cells attain a maximum temperature of 302.149 K for a Reynolds number of 1200.

Figure 5.3 (c) shows that, while the maximum cell temperature has reached 302.040 K, the average temperature of 40 cells has decreased for a Reynolds number of 1500.

Figure 5.3 (d) shows that the three cells reached a maximum temperature of 301.891 K at a Reynolds number of 1800.

Figure 5.3 (e) indicates that the maximum temperature of the cells has reached 301.830 K, with very little variation as the Reynolds number is increased further.

5.2.1 Parametric study of Result of Maximum Temperature (T_{max}) for 4C drain rate

- Most extreme temperature keeps on diminishing on expanding the stream rate / Reynolds no.
- Additionally, the foremost extraordinary temperature appears a striking increase with higher coolant outlet temperature (T_c), which alters with the revelations from the past affectability examination.
- As a result, in arrange to move forward the warm dissemination adequacy of the Battery warm administration, it is suggested to prioritize bringing down the cooling liquid temperature at the section of discuss and raising its speed of the approaching coolant stream.
- At the same time, decreasing the thickness of the cooling plate divider can to progress the by and large cooling effectiveness of the framework.

The least most extreme temperature = 300.183K for $Re=2100$

Fig. 5.4 (a) shows the pressure distribution of fluid channel for $Re = 900$ & Fig. 5.4 (b) shows the pressure distribution of fluid channel for $Re = 1200$. Subsequently, Fig. 5.4 (c) shows the pressure distribution of fluid channel for $Re = 1500$, Fig. 5.4 (d) shows the pressure distribution of fluid channel for $Re = 1800$ & Fig. 5.4 (e) pressure distribution of fluid channel for $Re = 2100$

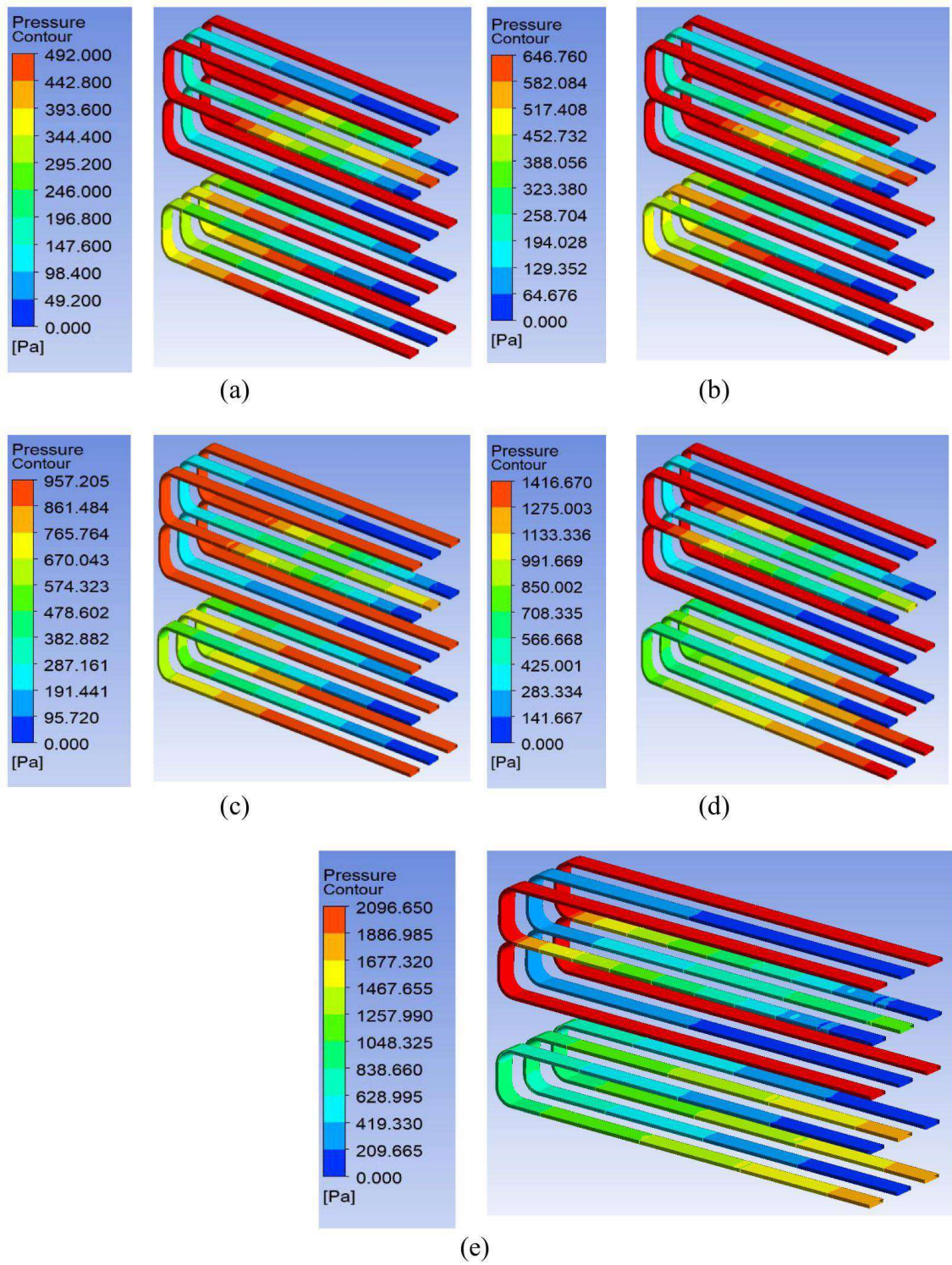


Fig. 5.4 Pressure drop of fluid channel during 4C drain rate for (a) $R_e = 900$, (b) $R_e = 1200$, (c) $R_e = 1500$, (d) $R_e = 1800$, (e) $R_e = 2100$

Figure 5.4 (a) shows that the pressure is highest at the intake sections, with a maximum pressure of 437 Pa achieved at a 3C drain rate for a Reynolds number of 900. It is also shown here that the pressure is higher at the curve sections due to the additional component of bend friction losses.

Figure 5.4 (b) indicates that as the Reynolds number increases by 300, the maximum pressure reached rises to 646.76 Pa for a Reynolds number of 1200.

Figure 5.4 (c) shows that while the maximum pressure has reached 957.205 Pa, the pressure at the front inlet sections is lowered for a Reynolds number of 1500.

Maximum pressure has grown up to 1416.67 Pa for Reynolds number of 1800, as shown in Figure 5.4 (d).

Figure 5.2 (e) indicates that the maximum pressure has increased to 2096.65 Pa, whereas the pressure at the front intake sections has decreased for a Reynolds number of 2100.

5.2.2 Parametric study of Result of Pressure Drop (ΔP) for 4C

- As we will watch from the weight forms that as the stream rate is expanded at higher Reynolds no.
- • The weight drop is expanded due to extend within the speed and stream rate of liquid i.e., water in this case. For 3C release rate the most extreme weight is at higher Reynolds no. = 2100 which is rise to 2096 Pa.
- • Furthermore, the weight drop may be a work of grinding calculate and thus we are able conclude that the expanded stream rate and speed of liquid increments the contact within the liquid channel which assist increments the weight drop.
- • Additionally, the expanded weight drop increments the pumping control required for the liquid or coolant which also increments the taken a toll.
- • Additionally, we are able watch that the most extreme weight drop is watched the admissions areas

5.2.3 Parametric study of fluid outlet temperature ($T_{c,out}$)

- As observed from the results, increasing the flow rate and a higher Reynolds number increases heat dissipation from the surface to the fluid channel via conduction and then convection mode of heat transfer, and thus the fluid outlet temperature increases.

- The maximum fluid outlet temperature observed for 4C discharge rate is 384.96K at $Re = 2100$ for 4C drain rate.

5.3 COMPARISON OF MAXIMUM TEMPERATURE (T_{max}) OF CELL SURFACE WITH VARYING REYNOLDS NO. FOR 3C & 4C DISCHARGE RATE

Fig. 5.5 shows comparison of maximum temperature of cell surface with varying Reynolds no. for 3c & 4c discharge rate

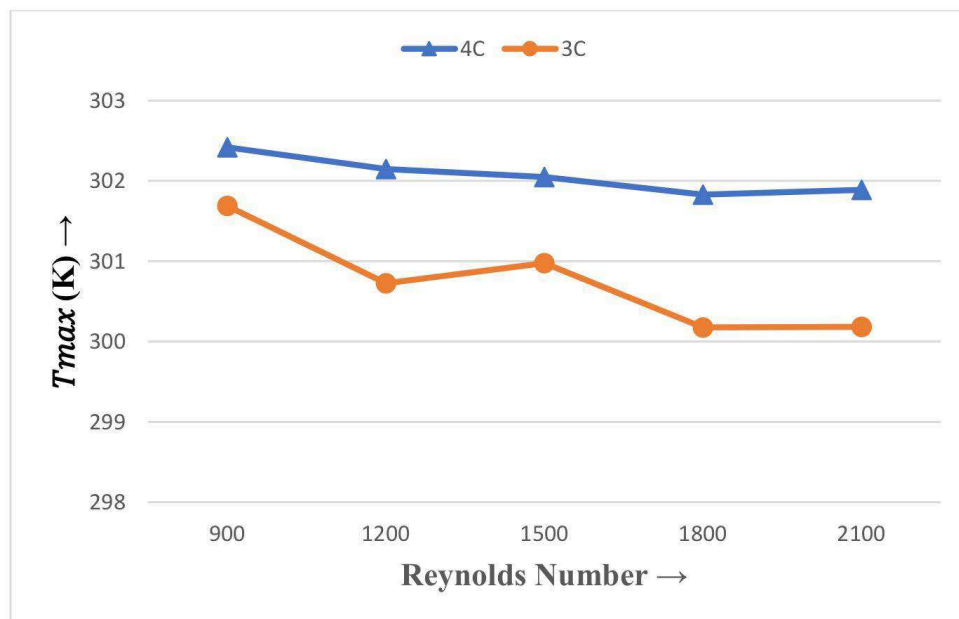


Fig. 5.5 Comparison of maximum temperature of cell by varying Reynolds number

5.3.1 Explanation of results:

The results clearly show that the maximum temperature for 3c and follow a decreasing pattern with Reynolds number ad. Heat dissipation increases as flow velocity increases due to higher flow rate. When cooling fluid flows from input to outlet, it undergoes heating. Consequently, if the coolant is directed to flow in the same direction through all the cooling plates, the cooling plate at the outlet end will be hotter. As a result, the cells located near the outlet will experience a relatively poorer cooling rate, leading to higher peak temperatures within the battery pack. However, in cases where the coolant flows in both directions, these cells are no longer exposed to the hotter regions of the cooling plate. This results in a decrease in the peak temperature compared to case of uni-direction flow.

Furthermore, when the coolant flows in both directions, both ends of the cooling plates will have almost the same temperature. As a result, cells at both ends will experience a similar cooling effect.

5.4 COMPARISON OF TC (COOLANT OUTLET) TEMP WITH VARYING REYNOLDS NO. FOR 3C & 4C DISCHARGE RATE

Fig. 5.6 shows comparison of coolant outlet temp with varying Reynolds no. for 3c & 4c discharge rate

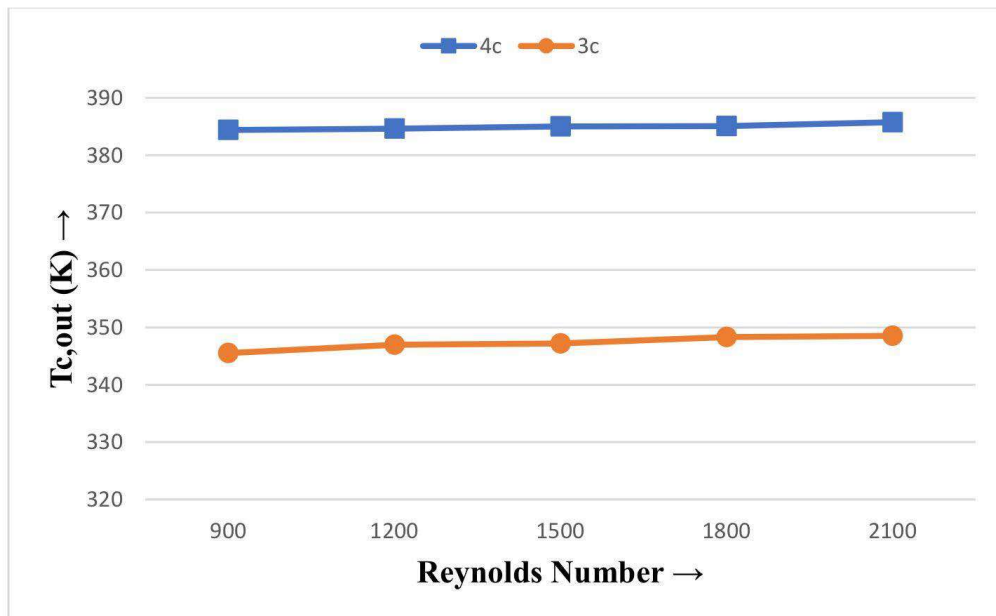


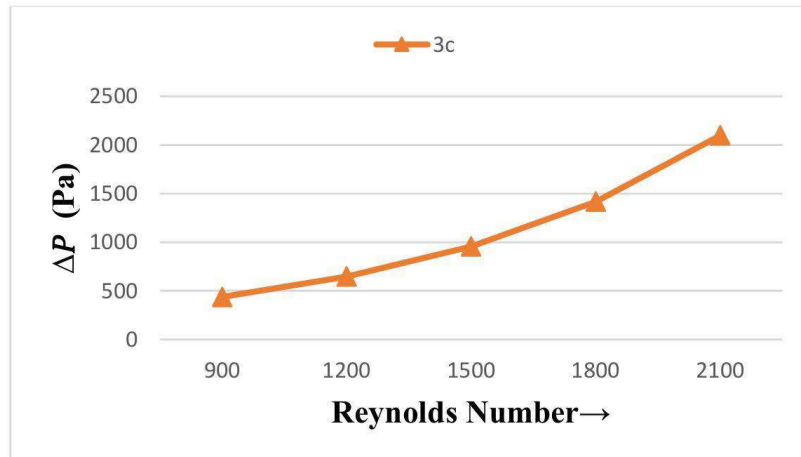
Fig. 5.6 Comparison of fluid outlet temperature by varying Reynolds number

5.4.1 Explanation of Results

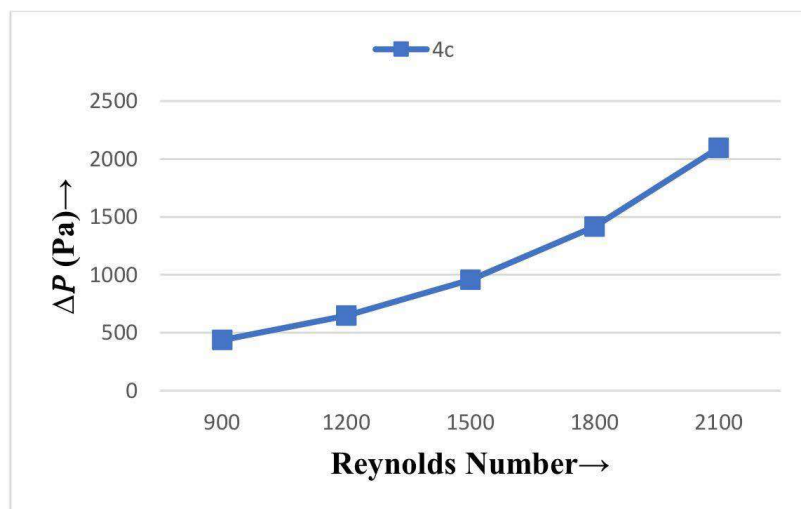
The heat dissipation rate increases with flow velocity and decreases with coolant temperature. The coolant temperature at the output is higher than the inlet in both 3C and 4C scenarios. The coolant velocity at the outflow of converging channels is greater than at the entrance. Taking both factors into account, the heat removal from regions near the inlet and outlet will be nearly equal in converging channels, resulting in better temperature uniformity. However, in the diverging channel, the outlet region of the mini-channel will have slower and hotter coolant, which leads to poorer heat dissipation.

5.5 COMPARISON OF P.D (PRESSURE DIFFERENCE PA) OF FLUID / COOLANT WITH VARYING FLOW RATE / REYNOLDS NO. FOR 3C (Fig. 5.3 a) & 4C (Fig. 5.3 b) DISCHARGE RATE

Fig. 5.3 (a) shows comparison of Pressure difference for increasing Reynolds number for 3C drain rate (b) shows comparison of Pressure difference for increasing Reynolds number for 4C drain rate



(a)



(b)

Fig. 5.7 Comparison of pressure difference for 3C and 4C drain rate with varying Reynolds number

5.5.1 Explanation of Results

The liquid pressure drop increases with increasing flow rate and Reynolds number for both 3C and 4C discharge. However, raising the flow rate reduces the maximum temperature while increasing the pumping power. The pressure drop can be minimized by increasing the thickness of the cooling channel as a result of an increase in t_2 (coolant temperature at the output) and v (coolant velocity). Furthermore, lowering t_1 (coolant temperature at the inlet) and correspondingly lowering the coolant flow rate at the air inlet can help to reduce system pressure drop.

CHAPTER 6

CONCLUSIONS

This thesis study proposes a unique liquid cooling method for a lithium-ion battery module consisting of 40 cylindrical cells using mini-channel cooling plates. In this study, staggered arrangements of lithium-ion cells were investigated for coolant intake and outlet passage. To improve heat dissipation performance, the cooling plates are positioned vertically along the height of the cells in a U-shaped pattern while tapping four spots, and liquid water is used as the coolant. The following conclusions can be reached:

- The use of coolant flow in both directions provides improved cooling performance and temperature consistency in comparison to condition where coolant flows in the same direction in all channels and having only single U channel.
- At higher flow rate this novel design able to limit maximum temperature to 301.89 K & 300.183 for 4C & 3C discharge rate respectively.
- At an increased flow rate and at higher Reynolds no. there is negligible change observed at maximum temperature and fluid outlet temperature.
- There is no much change in the pressure difference for 3C and 4c discharge rate since the pressure difference is a function of friction factor and velocity which remains unchanged for constant flow rate.
- However, by increasing the flow rate the pressure difference is increased which additionally increase the pumping power required to flow the fluid/coolant.
- The temperature of the coolant is critical in determining the highest increase in temperature (57.97%) within the battery, while having little impact on the degree of temperature homogeneity throughout the battery's surface. Furthermore, it has essentially no effect on the planned cell thermal management voltage decrease.

- Increasing the thickness of the cooling channel is recommended to improve the cell thermal management system thermal dissipation performance while minimizing the aforementioned factors.
- Increasing the width of the cooling channel is recommended to increase the cell thermal management thermal dissipation performance and alleviate the aforementioned problems.

REFERENCES

- [1] S. J. Skerlos and J. J. Winebrake, "Targeting plug-in hybrid electric vehicle policies to increase social benefits," *Energy Policy*, vol. 38, no. 2 February, pp. 705-708, 2010.
- [2] C. Zhao, W. Cao, T. Dong and F. Jiang, "Thermal behavior study of discharging/charging cylindrical lithium-ion battery module cooled by channeled liquid flow," *International Journal of Heat and Mass Transfer*, vol. 120, pp. 751-762, 2018.
- [3] R. Spotnitz and J. Franklin, "Abuse behavior of high-power, lithium-ion cells," *Journal of Power Sources*, vol. 113, no. 1, pp. 81-100, 2003.
- [4] T. M. Bandhauer, S. Garimella and T. F. Fuller, "A Critical Review of Thermal Issues in Lithium-Ion Batteries," *Journal of The Electrochemical Society*, vol. 158, no. 3, p. 2011
- [5] J.-c. Zhao, S.-h. Liu and J.-f. Zhang, "Personalized Distance Learning System based on Sequence Analysis Algorithm," *International journal of online and biomedical engineering*, vol. 11, no. 7, 2014.
- [6] W. Li, A. Garg, M. Xiao and L. Gao, "Optimization for Liquid Cooling Cylindrical Battery Thermal Management System Based on Gaussian Process Model," *Journal of thermal science and engineering applications*, vol. 13, no. 2, 2021.
- [7] A. Greco, D. Cao, X. Jiang and H. Yang, "A theoretical and computational study of lithium-ion battery thermal management for electric vehicles using heat pipes," *Journal of Power Sources*, vol. 257, pp. 344-355, 2014.
- [8] W. Li, A. Jishnu, A. Garg, M. Xiao, X. Peng and L. Gao, "Heat Transfer Efficiency Enhancement of Lithium-Ion Battery Packs by Using Novel Design

of Herringbone Fins,” *Journal of thermal science and engineering applications*, vol. 17, no. 2, 2020.

- [9] A. Garg, C. Liu, A. K. Jishnu, L. Gao, M. L. Le Phung and V. M. Tran, “A Thompson Sampling Efficient Multi-Objective Optimization Algorithm (TSEMO) for Lithium-Ion Battery Liquid-Cooled Thermal Management System: Study of Hydrodynamic, Thermodynamic, and Structural Performance,” *journal of thermal science and engineering applications*, vol. 18, no. 2, 2021.
- [10] J. Kim, J. Oh and H. Lee, “Review on battery thermal management system for electric vehicles,” *Applied Thermal Engineering*, vol. 149, pp. 192-212, 2019.
- [11] L. Cheng, A. Garg, A. Jishnu and L. Gao, “Surrogate based multi-objective design optimization of lithium-ion battery air-cooled system in electric vehicles,” *Journal of Energy Storage*, vol. 31, 2020.
- [12] N. Wang, C. Li, W. Li, M. Huang and D. Qi, “Effect analysis on performance enhancement of a novel air cooling battery thermal management system with spoilers,” *Applied Thermal Engineering*, vol. 192, p. 116932, 2021.
- [13] S. A. Hallaj and J. R. Selman, “A Novel Thermal Management System for Electric Vehicle Batteries Using Phase-Change Material,” *Journal of The Electrochemical Society*, vol. 147, no. 9, pp. 3231-3236, 2000.
- [14] N. Javani, I. Dincer, G. Naterer and G. Rohrauer, “Modeling of passive thermal management for electric vehicle battery packs with PCM between cells,” *Applied Thermal Engineering*, vol. 73, no. 1, pp. 307-316, 2014.
- [15] Y. Wei and M. Agelin-Chaab, “Experimental investigation of a novel hybrid cooling method for lithium-ion batteries,” *Applied Thermal Engineering*, vol. 136, pp. 375-387, 2018.

- [16] X. Yuan, A. Tang, C. Shan, Z. Liu and J. Li, "Experimental investigation on thermal performance of a battery liquid cooling structure coupled with heat pipe," *Journal of Energy Storage*, vol. 32, p. 101984, 2020 .
- [17] C. Zhao, A. C.M. Sousa and F. Jiang, "Minimization of thermal non-uniformity in lithium-ion battery pack cooled by channeled liquid flow," *International Journal of Heat and Mass Transfer*, vol. 129, pp. 660-670, 2019.
- [18] M. Malik, I. Dincer, M. A. Rosen, M. Mathew and M. Fowler, "Thermal and electrical performance evaluations of series connected Li-ion batteries in a pack with liquid cooling," *Applied Thermal Engineering*, vol. 129, pp. 472-481, 2018.
- [19] J. Liang, Y. Gan, Y. Li, M. Tan and J. Wang, "Thermal and electrochemical performance of a serially connected battery module using a heat pipe-based thermal management system under different coolant temperatures," *Energy*, vol. 189, p. 116233, 2019.
- [20] M. Al-Zareer, I. Dincer and M. A. Rosen, "A review of novel thermal management systems for batteries," *International journal of energy research*, vol. 42, no. 10, pp. 3182-3205, 2018.
- [21] Y. Lai, W. Wu, K. Chen, S. Wang and C. Xin, "A compact and lightweight liquid-cooled thermal management solution for cylindrical lithium-ion power battery pack," *International Journal of Heat and Mass Transfer*, vol. 144, p. 118581, 2019.
- [22] J. Zhao, Z. Rao and Y. Li, "Thermal performance of mini-channel liquid cooled cylinder based battery thermal management for cylindrical lithium-ion power battery," *Energy Conversion and Management*, vol. 103, pp. 157-165, 2015.
- [23] D. Bernardi, E. Pawlikowski and J. Newman, "A General Energy Balance for Battery Systems," *Journal of The Electrochemical Society*, vol. 132, no. 1, 1985.

- [24] Z. Rao, Z. Qian, Y. Kuang and Y. Li, "Thermal performance of liquid cooling based thermal management system for cylindrical lithium-ion battery module with variable contact surface," *Applied Thermal Engineering*, vol. 123, pp. 1514-1522, 2017.
- [25] R. Pakrouh, M. Hosseini, R. Bahrampoury, A. Ranjbar and S. Borhani, "Cylindrical battery thermal management based on microencapsulated phase change slurry," *Journal of Energy Storage*, vol. 40, p. 102602, 2021,.
- [26] C. Zhao, W. Cao, T. Dong and F. Jiang, "Thermal behavior study of discharging/charging cylindrical lithium-ion battery module cooled by channeled liquid flow," *International Journal of Heat and Mass Transfer*, vol. 120, pp. 751-762, 2018.
- [27] H. Zhou, F. Zhou, Q. Zhang, Q. Wang and Z. Song, "Thermal management of cylindrical lithium-ion battery based on a liquid cooling method with half-helical duct," *Applied Thermal Engineering*, vol. 162, p. 114257, 2019 .
- [28] Y. Huang, Y. Lu, R. Huang, J. Chen, F. Chen, Z. L. X. Yu and A. Paul Roskilly, "Study on the thermal interaction and heat dissipation of cylindrical Lithium-Ion Battery cells," *Energy Procedia*, vol. 142, pp. 4029-4036, 2017.
- [29] L. Huat Saw, Y. Ye, A. A.O. Tay, W. Tong Chong, S. How Kuan and M. Chian Yew, "Computational fluid dynamic and thermal analysis of Lithium-ion battery pack with air cooling," *Applied Energy*, vol. 177, pp. 783-792, 2016.
- [30] T. Wang, K. Tseng and J. Zhao, "Development of efficient air-cooling strategies for lithium-ion battery module based on empirical heat source model," *Applied Thermal Engineering*, vol. 90, pp. 521-529, 2015.
- [31] B. Ye, M. R. Haque Rubel and H. Li, "Design and Optimization of Cooling Plate for Battery Module of an Electric Vehicle," *Applied Sciences*, p. 754, 2019.